



## Research paper

## Deoxygenation of methyl laurate as a model compound on Ni-Zn alloy and intermetallic compound catalysts: Geometric and electronic effects of oxophilic Zn

Zhengyi Pan, Rijie Wang, Jixiang Chen\*

Tianjin Key Laboratory of Applied Catalysis Science and Technology, Department of Catalysis Science and Engineering, School of Chemical Engineering and Technology, Tianjin University, Tianjin 300072, China

## ARTICLE INFO

## Keywords:

Ni-Zn alloy/intermetallic compound  
Decarbonylation/decarboxylation  
Hydrodeoxygenation  
C–C bond hydrogenolysis  
Methanation

## ABSTRACT

A series of Ni-Zn bimetallic catalysts with different Ni/Zn atomic ratios were prepared from layered double hydroxides (LDHs) with an atomic ratio of 3 between divalent ( $\text{Ni}^{2+}$  and  $\text{Zn}^{2+}$ ) and trivalent ions ( $\text{Al}^{3+}$ ). After the mixed oxides derived from calcined LDHs were reduced with  $\text{H}_2$  at 650 °C, Ni-rich alloy with a fcc structure was synthesized at Ni/Zn ratios  $\geq 2$ , while an Ni-Zn intermetallic compound (IMC) with a tetragonal  $\text{L1}_0$  structure was generated at Ni/Zn atomic ratios of 1 and 1/2, and an Ni-Zn IMC was generated with a cubic structure at Ni/Zn ratio of 1/8. HAADF-STEM-EDS,  $\text{H}_2$  chemisorption and magnetic measurements showed that Ni and Zn atoms were uniformly distributed in catalysts, and the ensembles of Ni atoms decreased with decreasing Ni/Zn ratios. XPS and CO-TPD characterizations revealed a charge transfer from Ni to Zn. In the deoxygenation of methyl laurate as a model compound to diesel-like hydrocarbons, although the addition of Zn reduced the conversion of methyl laurate, mostly due to the decrease in Ni content, a synergetic effect between Ni and Zn was suggested to enhance turnover frequency (TOF), and higher TOFs were obtained on the catalysts with Ni/Zn ratios of 1/1 and 1/2. Because of the high oxophilicity of Zn, this synergetic effect also promoted the hydrodeoxygenation pathway. With decreasing Ni/Zn ratios, the molar ratio between  $\text{C}_{11}$  hydrocarbons and both  $\text{C}_{12}$  hydrocarbons and oxygenates decreased. Particularly, it was smaller than 0.2 on Ni-Zn IMC when the reaction temperature was 330 °C, and much lower than that of 60.5 on the metallic Ni catalyst. Compared with metallic Ni, Ni-rich alloys and IMCs (especially IMCs) showed lower reactivity for C–C bond hydrogenolysis and CO/ $\text{CO}_2$  methanation, which was more remarkable with decreasing Ni/Zn atomic ratios and increasing reaction temperatures. Particularly, when the conversion of methyl laurate was close to 100% at 400 °C, the metallic Ni catalyst dominantly gave methane, which was derived from C–C bond hydrogenolysis as well as complete methanation of CO/ $\text{CO}_2$ , and the total selectivity to  $\text{C}_{11}$  and  $\text{C}_{12}$  (i.e.,  $S_{\text{C}_{11}+\text{C}_{12}}$ ) was only 1.1%. However, when the Ni/Zn atomic ratio was  $\leq 2/1$ ,  $S_{\text{C}_{11}+\text{C}_{12}}$  reached as high as 96.2%, and the molar ratio between (CO +  $\text{CO}_2$ ) and  $\text{C}_{11}$  hydrocarbons was still larger than 1.0, i.e., C–C bond hydrogenolysis and methanation were remarkably suppressed on Ni-Zn IMC catalysts. We suggest that the role of Zn is ascribed to its geometric and electronic modification of Ni in the alloy and IMC.

## 1. Introduction

Recently, the deoxygenation of vegetable oils in an  $\text{H}_2$  atmosphere to diesel-like hydrocarbons has attracted great attention due to energy and environmental issues. Two deoxygenation pathways (i.e., hydrodeoxygenation (HDO) and decarbonylation/decarboxylation) that are closely related to catalyst properties and reaction conditions occur during deoxygenation [1,2–5].

Although conventional hydrotreating catalysts (e.g., sulfided NiMo and CoMo) have been widely investigated [1,2,6–8], it is very

interesting to develop non-sulfide catalysts because there is scarce sulfur in vegetable oil, while sulfur is necessary for maintaining sulfide catalyst stability. Noble metal catalysts have been found to show good performance for the deoxygenation of fatty acids and their esters [2,3], but they are a limited resource with very high cost.

Low-cost metallic Ni is a good alternative for the deoxygenation of fatty acids and their esters [4]. Unfortunately, its high reactivity for undesired C–C bond hydrogenolysis and methanation gives rise to low carbon yield and high  $\text{H}_2$  consumption [3,9,10]. Suppressing these undesired reactions is an interesting goal. A feasible approach is to

\* Corresponding author.

E-mail address: [jxchen@tju.edu.cn](mailto:jxchen@tju.edu.cn) (J. Chen).<http://dx.doi.org/10.1016/j.apcatb.2017.10.040>

Received 11 June 2017; Received in revised form 13 October 2017; Accepted 14 October 2017

Available online 16 October 2017

0926-3373/ © 2017 Elsevier B.V. All rights reserved.

modifying the structure of metallic Ni with a second less-reactive metal or non-metal (e.g., Fe, Cu, Mo and P). We have found that nickel phosphides possess much lower activity for C–C bond hydrogenolysis and methanation than metallic Ni due to the geometric and electronic effects of P [10,11]. Additionally, the formation of alloys and inter-metallic compounds (IMCs) is available for tailoring the structure of a single metal [12–14]. In the deoxygenation of fatty acid esters, compared with metallic Ni, NiFe alloys are more active for deoxygenation but less active for C–C bond hydrogenolysis, and they are more favorable to the HDO pathway due to the oxophilicity of Fe [15,16]. For instance, in the deoxygenation of methyl laurate at 360 °C [16], with increasing Fe/Ni atomic ratios from 0 to 0.25, the selectivity to the cracked products decreased from 67% to 2%, while the  $n\text{-C}_{11}/n\text{-C}_{12}$  molar ratio (denoting the selectivity between decarbonylation/decarboxylation and HDO pathways) decreased from  $\sim 44$  to 2. Compared with decarbonylation/decarboxylation, the HDO pathway gives rise to high carbon yield. However, the NiFe alloy still shows high reactivity for methanation [16,17]. Loe et al. [18] reported that Ni-Cu/Al<sub>2</sub>O<sub>3</sub> showed superior reactivity to Ni/Al<sub>2</sub>O<sub>3</sub> in the deoxygenation of tristearin and stearic acid, and found that the Ni-Cu alloy is less reactive for C–C bond cleavage and methanation than metallic Ni [18,19]. Different from the oxophilic Fe, Cu has a minor effect on deoxygenation pathways, i.e., Ni-Cu bimetallic catalysts still prefer to catalyze decarbonylation/decarboxylation [18,19]. Interestingly, the introduction of oxophilic Mo into Ni-Cu/Al<sub>2</sub>O<sub>3</sub> not only enhanced catalyst reactivity but also promoted the HDO pathway [20]. In [20], the performance of Ni-Cu and Ni-Mo catalysts was also compared. At 300 °C and 0.25 MPa H<sub>2</sub>, in the deoxygenation of the mixture of ethyl caprate and methyl palmitate, the Ni-Mo catalyst produced higher conversion (90%) than the Ni-Cu catalyst (60%). For the Ni-Mo catalyst, the total selectivity to C<sub>9</sub>H<sub>20</sub> and C<sub>15</sub>H<sub>32</sub> (i.e., products from decarbonylation/decarboxylation) and that to C<sub>10</sub>H<sub>22</sub> and C<sub>16</sub>H<sub>34</sub> (i.e., products from HDO) were 31% and 54%, respectively. However, for the Ni-Cu catalyst, the total selectivity to C<sub>9</sub>H<sub>20</sub> and C<sub>15</sub>H<sub>32</sub> and that to C<sub>10</sub>H<sub>22</sub> and C<sub>16</sub>H<sub>34</sub> were 77.3% and 2.8%, respectively. Clearly, the Ni-Mo catalyst favored the HDO pathway more than the Ni-Cu catalyst.

Recently, metallic Zn has been found to exhibit interesting effects on the reactivity of Ni and Pt catalysts in some reactions. In the hydrogenolysis of glycerol, ZnNiAl catalysts exhibit higher reactivity and selectivity to 1,2-propanediol and less reactivity for C–C bond cleavage than NiAl due to the formation of Ni-Zn alloys [21]. Vohs et al. [22,23] found that, in the deoxygenation of aldehydes and furfural, Pt(111) favors the formation of acyl intermediates those readily undergo decarbonylation, while Zn/Pt(111) stabilizes an  $\eta^2(\text{C},\text{O})$  configuration of aldehyde carbonyl where the O is bonded to an oxophilic Zn site and the C to a Pt site, and thus the HDO pathway is facilitated. In liquid phase selective hydrogenation of citral, the addition of ZnO into the Ni/C catalyst improved selectivity toward citronellol [24]. Although no Ni-Zn alloy was formed, a ZnO–Ni interaction is suggested to be responsible for the activation of the C=O bond in the citral molecule.

From the above, we speculate that, in Ni-based catalysts, introducing another less reactive metal for C–C bond hydrogenolysis and methanation while using a more oxophilic metal might be promising for suppressing the C–C bond hydrogenolysis and methanation while promoting the HDO pathway in the deoxygenation of fatty acids and their esters. Based on this, Zn is a good candidate. Some researchers have reported the “ligand” (or electronic) and/or “ensemble” (or geometric) effects of Zn on Ni in Ni-Zn alloys and IMCs [21,25,26]. Ni-Zn IMCs have been found to suppress methanation in the steam reforming of methanol [25]. The formation of Ni-Zn alloys has been found to promote C–O cleavage while suppressing C–C bond hydrogenolysis in the hydrogenolysis of glycerol [21]. To the best of our knowledge, the deoxygenation of fatty acid esters on Ni-Zn alloy and IMC catalysts has not been reported. We believe that it is worth studying the relationship between the structure and performance of Ni-Zn alloys and IMCs, which will provide valuable information for the design of efficient Ni-based

catalysts for deoxygenation of fatty acid esters to diesel-like hydrocarbons.

In the present work, to explore the effect of Zn on the performance of metallic Ni for the deoxygenation of methyl laurate as a model compound to diesel-like hydrocarbons, we prepared Ni-Zn alloys and IMC catalysts with different Ni/Zn atomic ratios. Given that the composition of the layered double hydroxide (LDH) can be well-controlled, and the divalent and trivalent metal ions in the basal layers of LDH uniformly disperse and mix at the atomic level [27–29], the LDH precursor was selected to prepare Ni-Zn alloys and IMC catalysts. Interestingly, compared with metallic Ni, the Ni-Zn alloy and IMC, especially the IMC, were found to have much lower reactivities for C–C bond hydrogenolysis and methanation and favored the HDO pathway more, which is very positive because the carbon yield was increased while H<sub>2</sub> consumption was decreased. Finally, we analyze the relationship between the catalyst structure and reactivity in detail and suggest that the performance of Ni-Zn alloys and IMCs should be ascribed to the geometric effect, electronic effect and oxophilicity of Zn.

## 2. Experimental

### 2.1. Catalyst preparation

The bimetallic Ni-Zn alloy and IMC catalysts were prepared from the layered double hydroxides using the three steps described below. The dosage of metal nitrate salts and nominal composition of the prepared catalysts with different Ni/Zn ratios are listed in Table S1 in Supplementary information. 1) Coprecipitation was followed by drying at 70 and 100 °C to produce the layered double hydroxide (LDH) precursor (labeled as Ni<sub>x</sub>Zn<sub>y</sub>Al-LDH, where x/y denotes the Ni/Zn atomic ratio). 2) The calcination of Ni<sub>x</sub>Zn<sub>y</sub>Al-LDH was performed at 500 °C to produce mixed metal oxide (labeled as Ni<sub>x</sub>Zn<sub>y</sub>Al-O). As indicated in Section 3.1.2, Al<sup>3+</sup> existed in the form of Al<sub>2</sub>O<sub>3</sub> and/or ZnAl<sub>2</sub>O<sub>4</sub>. 3) The reduction of Ni<sub>x</sub>Zn<sub>y</sub>Al-O was performed at 650 °C, during which Ni and Zn species could be reduced to Ni-Zn bimetallic catalysts (labeled as Ni<sub>x</sub>Zn<sub>y</sub>Al). It is necessary to note that, to avoid drastic oxidation, the prepared Ni<sub>x</sub>Zn<sub>y</sub>Al catalyst after reduction at 650 °C was passivated at room temperature in a 0.5 vol% O<sub>2</sub>/N<sub>2</sub> flow (320 mL/min) for 4 h before the catalytic test and characterization. The details for catalyst preparation are available in the Supplementary information.

### 2.2. Catalyst characterization

N<sub>2</sub> sorption, XRD and UV–vis were adopted to characterize the textural and structural properties of catalysts. H<sub>2</sub>-TPR and CO-TPD were used to investigate the reducibility of Ni<sub>x</sub>Zn<sub>y</sub>Al-O samples and the interaction between CO and Ni sites on Ni<sub>x</sub>Zn<sub>y</sub>Al catalysts, respectively. The density of surface Ni sites was measured by H<sub>2</sub> chemisorption. The details for these characterizations are available in the Supplementary information.

Transmission electron microscopy (TEM) and high-angle annular dark-field scanning transmission electron microscopy (HAADF-STEM) line scans combined with energy dispersive X-ray spectroscopy (EDX) were carried out on a JEOL JEM-2100F instrument (200 kV). The magnetic properties of the passivated Ni<sub>x</sub>Zn<sub>y</sub>Al catalysts were measured on a quantum design physical properties measurement system (PPMS-9) at 27 °C. X-ray photoelectron spectroscopy (XPS) was performed on a PHI 5000VersaProbe instrument with Al K $\alpha$  radiation (1486.6 eV). Binding energies were determined with adventitious carbon (C1s at 284.8 eV) as the reference. Before measurement, the passivated catalysts were sputter-cleaned with an Ar<sup>+</sup> ion beam (4 kV, 25 mA) for 3 min.

### 2.3. Catalytic test

The catalyst reactivity for the deoxygenation of methyl laurate was

evaluated on a continuous-flow stainless-steel fixed-bed reactor (inner diameter of 12 mm). In the blank reactor, a very low conversion of methyl laurate (< 1% even at 400 °C) indicates a small influence of the reactor itself on the deoxygenation reaction. For this process, 0.08 g passivated  $\text{Ni}_x\text{Zn}_y\text{Al}$  catalyst (0.15–0.25 mm in diameter) diluted with 3 g quartz sand with the same size was loaded into the reactor. Then, 2 g quartz sand was put on the catalyst bed. Before the test, the passivated catalyst was re-reduced at 450 °C for 1 h in a  $\text{H}_2$  flow (> 99.9%, 100 mL/min), and then the temperature and the  $\text{H}_2$  pressure were adjusted to 330 or 400 °C and 3.0 MPa, respectively. Subsequently, methyl laurate was fed into the reactor with a liquid micro pump. Unless stated, the  $\text{H}_2$ /methyl laurate molar ratio and the weight hourly space velocity of methyl laurate were set as 25 and  $70 \text{ h}^{-1}$ , respectively. During the reaction, the catalyst bed was isothermal, and the reaction was operated in the absence of heat/mass transfer limitations, as indicated in the Supplementary information. The mass balance exceeded 97%. The liquid samples were identified by gas chromatograph (GC) standards with an Agilent GC6890-MS5973N. The liquid samples were quantitatively analyzed on a SP-3420 GC equipped with a flame ionization detector (FID) and a HP-5 capillary column ( $30 \text{ m} \times 0.32 \text{ mm} \times 0.5 \mu\text{m}$ ). Tetrahydronaphthalene (used as an internal standard) was added into the liquid sample to quantitatively analyze the concentration of each component.  $\text{CO}$ ,  $\text{CO}_2$  and  $\text{CH}_4$  in gaseous effluent were quantitatively analyzed on an on-line 102 GC equipped with a TCD and a TDX-101 packed column.  $\text{N}_2$  (used as an internal standard) was added into gaseous effluent. The representative chromatograms of liquid samples from SP-3420 GC and gaseous samples from 102 GC are shown in Fig. S1 in Supplementary information. The gaseous hydrocarbon products were detected on an on-line SP-3420 GC equipped with an FID and an HP-AL/S capillary column ( $50 \text{ m} \times 0.535 \text{ mm} \times 15 \mu\text{m}$ ).

The conversion of methyl laurate ( $X$ ) and the selectivity to product  $i$  ( $S_i$ ) are calculated by the following formulas:

$$X = (n_0 - n)/n_0 \times 100\%; S_i = n_i/(n_0 - n) \times 100\%$$

where  $n_0$  and  $n$  denote the moles of methyl laurate in feedstock and products, respectively, and  $n_i$  is the mole of product  $i$ .

Similar to previous work [30], the turnover frequency (TOF) of methyl laurate is calculated as follows:

$$\text{TOF} = -F \ln(1 - X)/(W \cdot 2M)$$

where  $F$  is the amount of methyl laurate fed to the reactor per second ( $\mu\text{mol/s}$ ),  $X$  is the conversion of methyl laurate,  $W$  is the catalyst weight (g) and  $M$  is  $\text{H}_2$  uptake ( $\mu\text{mol/g}$ ). This formula was used because the conversions were higher than 50% and even close to 100%, which were far from differential conditions, and so an integral analysis was required [31]. This formula, in which  $-\ln(1-X)$  substitutes for  $X$ , assumes a pseudo first-order reaction, which is reasonable because of the large excess of hydrogen and the isothermal catalyst bed.

### 3. Results

#### 3.1. Catalyst characterization

##### 3.1.1. $\text{Ni}_x\text{Zn}_y\text{Al}$ -LDH samples

As shown in the XRD patterns (Fig. S2 in Supplementary information), only diffraction peaks due to typical LDH are observed, implying a pure, well-crystallized LDH structure in all  $\text{Ni}_x\text{Zn}_y\text{Al}$ -LDH samples. The detailed structural properties of  $\text{Ni}_x\text{Zn}_y\text{Al}$ -LDH are shown in Table S2 in Supplementary information.

##### 3.1.2. $\text{Ni}_x\text{Zn}_y\text{Al}$ -O samples

$\text{Ni}_x\text{Zn}_y\text{Al}$ -Os samples were characterized by means of UV-vis DRS, XRD and  $\text{H}_2$ -TPR to obtain information about phase composition and reducibility.

The XRD patterns (Fig. S3) show that the peaks at  $2\theta = 37.2$ ,  $43.3$  and  $62.9^\circ$  due to rhombohedral NiO (PDF#44-1159) are observed for  $\text{Ni}_x\text{Zn}_y\text{Al}$ -Os (apart from  $\text{Ni}_0\text{Zn}_3\text{Al}$ -O and  $\text{Ni}_1\text{Zn}_8\text{Al}$ -O), and they slightly shifted to low angles with the decrease in the Ni/Zn ratio. This process should be ascribed to the incorporation of  $\text{Zn}^{2+}$  ions into bulk NiO because the radius of  $\text{Zn}^{2+}$  (0.074 nm) is larger than that of  $\text{Ni}^{2+}$  (0.069 nm) [32]. That is, an NiO-ZnO oxide solid solution formed in  $\text{Ni}_x\text{Zn}_y\text{Al}$ -Os. When the Ni/Zn ratios were  $\leq 1/1$ , hexagonal ZnO was detected. Additionally, the existence of  $\text{ZnAl}_2\text{O}_4$  cannot be ruled out in  $\text{Ni}_1\text{Zn}_2\text{Al}$ -O,  $\text{Ni}_1\text{Zn}_8\text{Al}$ -O and  $\text{Ni}_0\text{Zn}_3\text{Al}$ -O because the diffraction peaks due to  $\text{ZnAl}_2\text{O}_4$  are located at  $2\theta$  very close to those of ZnO apart from the peak at  $2\theta = 34.4^\circ$ . In fact,  $\text{ZnAl}_2\text{O}_4$  was detected in the reduced samples (Fig. 2). Additionally, no diffraction peaks due to alumina indicate its amorphous state and high dispersion. In the reduced Ni-Zn bimetallic catalysts as indicated in the next section,  $\text{Al}_2\text{O}_3$  acted as the support. In addition to  $\text{Ni}_1\text{Zn}_8\text{Al}$ -O and  $\text{Ni}_0\text{Zn}_3\text{Al}$ -O, other samples had similar NiO crystallite sizes (3.2–3.6 nm) (Table S3). Such small NiO crystallites are attributed to their derivation from the LDH precursors where the nickel species were uniformly mixed at atomic levels and highly dispersed. This process is also reflected by the UV vis DRS spectra of  $\text{Ni}_x\text{Zn}_y\text{Al}$ -O samples (Fig. S4), where the very weak peaks ascribed to the octahedrally coordinated  $\text{Ni}^{2+}$  in bulk NiO are visible at approximately 380, 410 and 720 nm [33]. Additionally, no peaks (600–640 nm) due to  $\text{NiAl}_2\text{O}_4$  are observed in UV vis DRS spectra [33].

Fig. 1 illustrates the  $\text{H}_2$ -TPR profiles of the  $\text{Ni}_x\text{Zn}_y\text{Al}$ -O samples. In the profile of  $\text{Ni}_3\text{Zn}_0\text{Al}$ -O, the main peak at 584 °C is ascribed to the reduction of NiO [34,35], but it was higher than that of free NiO (355 °C) (Fig. S5), indicative of a strong interaction between NiO and alumina [36]. In the profile of  $\text{Ni}_0\text{Zn}_3\text{Al}$ -O, the small peak at 645 °C is ascribed to the reduction of ZnO and  $\text{ZnAl}_2\text{O}_4$ . Such a small peak is ascribed to the high affinity of Zn to oxygen, making the reduction of ZnO difficult. For other  $\text{Ni}_x\text{Zn}_y\text{Al}$ -O samples, the peaks between 603 and 647 °C are attributed to the co-reduction of NiO and ZnO [32]. This finding is verified by the fact that the actual  $\text{H}_2$  consumption was larger than the theoretical consumption due to the reduction of only NiO (Table S3). Particularly, when Ni/Zn ratios were between 2/1 and 50/1, the actual  $\text{H}_2$  consumption ( $\sim 10.4 \text{ mmol/g}$ ) was even closer to the theoretical consumption due to the complete reductions of both NiO and ZnO (Table S3), i.e., NiO and ZnO were completely co-reduced.

In summary, NiO and NiO-ZnO solid solution crystallites were highly dispersed in  $\text{Ni}_x\text{Zn}_y\text{Al}$ -Os. During  $\text{H}_2$ -TPR process, NiO and ZnO could be simultaneously reduced, which facilitates the formation of Ni-

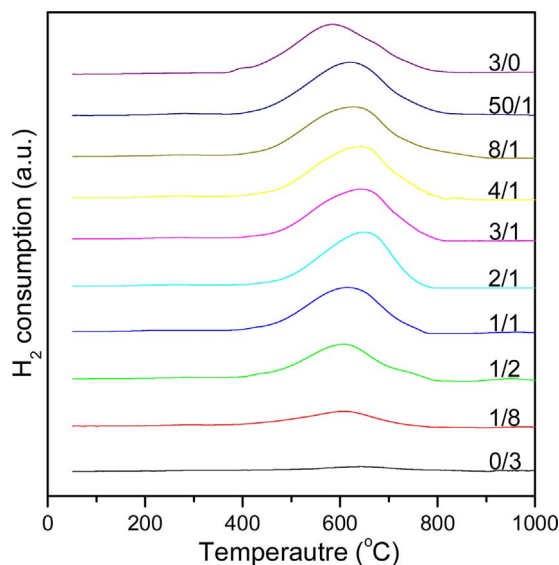


Fig. 1.  $\text{H}_2$ -TPR profiles of  $\text{Ni}_x\text{Zn}_y\text{Al}$ -O samples.  
Note: the number on the curve indicates Ni/Zn atomic ratio.

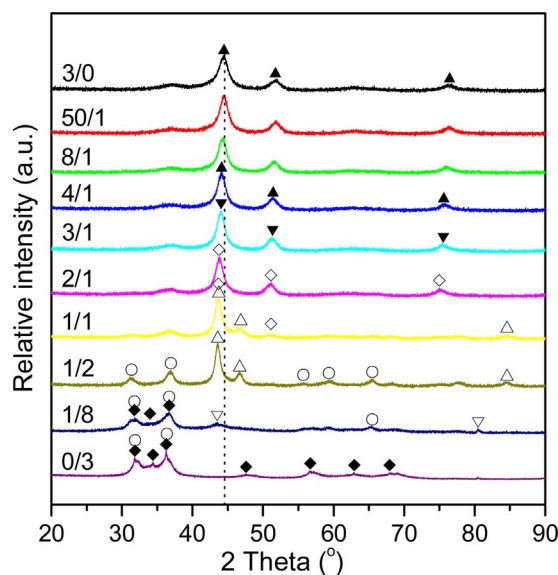


Fig. 2. XRD patterns of different  $\text{Ni}_x\text{Zn}_y\text{Al}$  catalysts.

Note: the number on the curve indicates the Ni/Zn atomic ratio;  $\blacktriangle$  Ni, PDF#04-0850;  $\blacktriangledown$   $\text{Ni}_4\text{Zn}$ ;  $\diamond$   $\text{Ni}_{70}\text{Zn}_{30}$ ;  $\triangle$  t-NiZn, PDF#06-0672;  $\nabla$  c-NiZn, PDF#65-3203;  $\circ$   $\text{ZnAl}_2\text{O}_4$ , PDF#05-0669;  $\blacklozenge$  ZnO, PDF#36-1451.

### Zn alloys and IMCs.

#### 3.1.3. $\text{Ni}_x\text{Zn}_y\text{Al}$ catalysts

**3.1.3.1. XRD, TEM and  $\text{N}_2$  sorption.** Fig. 2 presents the XRD patterns of  $\text{Ni}_x\text{Zn}_y\text{Al}$ . The peaks due to metallic Ni are visible at  $2\theta = 44.5$ ,  $51.8$  and  $76.4^\circ$  (PDF#04-0850) in the pattern of  $\text{Ni}_3\text{Zn}_0\text{Al}$ . In contrast, they shifted to low angles as the Ni/Zn atomic ratio decreased from 50/1 to 2/1. The lower the Ni/Zn ratio (i.e., the more the Zn content) was, the more obvious the shift. This finding is ascribed to the incorporation of the Zn atoms into the metallic Ni lattice to form the Ni-rich alloy, a substitutional solid solution with a face-centered cubic (fcc) structure (space group of Fm-3m) [37–39]. The Ni-rich alloy shows a lattice expansion compared with metallic Ni (Table 1). This finding is justified because the Zn atom has a larger radius (0.125 nm) than the Ni atom (0.115 nm). Particularly,  $\text{Ni}_4\text{Zn}$  and  $\text{Ni}_{70}\text{Zn}_{30}$  alloys formed in  $\text{Ni}_3\text{Zn}_1\text{Al}$  and  $\text{Ni}_2\text{Zn}_1\text{Al}$  [37,38,40], respectively. It is noteworthy that an IMC with tetragonal  $\text{L}_{10}$  structure (denoted as t-NiZn, space group of I4/mmm (139)), corresponding to the peaks at  $2\theta = 43.5$ ,  $46.7$  and  $84.4^\circ$  (PDF#06-0672), formed in  $\text{Ni}_1\text{Zn}_1\text{Al}$  and  $\text{Ni}_1\text{Zn}_2\text{Al}$ , and a cubic NiZn IMC (denoted as c-NiZn, space group of Pm-3m (221)) with peaks at  $2\theta = 43.5$ ,  $63.8$  and  $80.5^\circ$  (PDF#65-3203) formed in  $\text{Ni}_1\text{Zn}_8\text{Al}$ . In addition, the peaks due to  $\text{ZnAl}_2\text{O}_4$  and ZnO are visible in

the patterns of  $\text{Ni}_x\text{Zn}_y\text{Al}$  with the Ni/Zn ratio  $\leq 2/1$ . In short, the Ni-Zn alloy and IMCs (t-NiZn and c-NiZn) were synthesized in the  $\text{Ni}_x\text{Zn}_y\text{Al}$  catalysts, while their structure depended on the Ni/Zn ratios.

As indicated in Table 1, the average metallic Ni crystallite size in  $\text{Ni}_3\text{Zn}_0\text{Al}$  was 5.1 nm.  $\text{Ni}_x\text{Zn}_y\text{Al}$  (except for  $\text{Ni}_1\text{Zn}_8\text{Al}$ ) had larger Ni-Zn alloy and IMC crystallites, and the crystallite sizes increased from 5.3 to 9.0 nm with decreasing Ni/Zn ratios from 50/1 to 1/2. The incorporation of larger Zn atoms into the metallic Ni lattice may partially contribute to the increase in the alloy and IMC crystallite sizes. From this view point, the increased proportion of Zn in alloys and IMCs would give rise to larger crystallites.

Taking  $\text{Ni}_1\text{Zn}_1\text{Al}$  as an example, TEM was used to investigate catalyst morphology (Fig. 3(a)). The  $d$ -spacing value of 0.206 nm corresponds to the t-NiZn (101) crystal plane. The spherical t-NiZn particles distributed between 4 and 8 nm with an average particle size of 6.3 nm, consistent with that (6.7 nm) calculated from the XRD pattern (Table 1). Fig. 3(b) shows the HAADF-STEM image of a random area. The element mappings reveal that the Ni and Zn atoms are uniformly distributed in  $\text{Ni}_1\text{Zn}_1\text{Al}$ , which is also verified by a HAADF-STEM-EDS line scanning across a random area (Fig. 3(c)).

Table 1 shows the textural properties of the  $\text{Ni}_x\text{Zn}_y\text{Al}$  catalysts. Except for  $\text{Ni}_1\text{Zn}_1\text{Al}$  and  $\text{Ni}_1\text{Zn}_2\text{Al}$ , other  $\text{Ni}_x\text{Zn}_y\text{Al}$  catalysts had similar BET surface areas ( $100 \pm 10 \text{ m}^2/\text{g}$ ). With decreasing Ni/Zn ratios from 3/0 to 0/3, the pore volume and the average pore diameter increased from 0.3 to  $1.1 \text{ cm}^3/\text{g}$  and from 14 to 42 nm, respectively. The tendency for the increased pore diameters with decreasing the Ni/Zn ratios is visualized by the pore distributions (Fig. S6).

**3.1.3.2.  $\text{H}_2$  chemisorption and magnetic property.** Fig. 4 presents the  $\text{H}_2$  uptakes of  $\text{Ni}_x\text{Zn}_y\text{Al}$  catalysts.  $\text{Ni}_3\text{Zn}_0\text{Al}$  produced an  $\text{H}_2$  uptake of  $394 \mu\text{mol}/\text{g}$ , whereas no  $\text{H}_2$  uptake was measured for  $\text{Ni}_0\text{Zn}_3\text{Al}$ . That is, the surface Zn atoms were inactive for adsorbing  $\text{H}_2$ . The  $\text{H}_2$  uptake of  $\text{Ni}_{50}\text{Zn}_1\text{Al}$  was  $375 \mu\text{mol}/\text{g}$ , slightly less than that of  $\text{Ni}_3\text{Zn}_0\text{Al}$ . In contrast,  $\text{Ni}_8\text{Zn}_1\text{Al}$  produced much less  $\text{H}_2$  uptake ( $133 \mu\text{mol}/\text{g}$ ) than  $\text{Ni}_3\text{Zn}_0\text{Al}$ . It is noteworthy that, when the Ni/Zn atomic ratio was  $\leq 8/1$ , the  $\text{H}_2$  uptake shows a nearly linear decrease with decreasing Ni/Zn ratios. The  $\text{H}_2$  uptake of  $\text{Ni}_1\text{Zn}_8\text{Al}$  was only  $15 \mu\text{mol}/\text{g}$ . Clearly, the surface Zn atoms not only were inactive to hydrogen adsorption but also hindered the adsorption of hydrogen on surface Ni atoms. Given that the increase in crystallite sizes of Ni-Zn alloys and IMCs might be due to the incorporation of larger Zn atoms into the metallic Ni lattice, the nearly linear correlation between  $\text{H}_2$  uptake and Ni/Zn ratio may indicate that Ni and Zn atoms were homogeneously mixed and distributed on the surface of Ni-Zn alloys and IMC crystallites. In other word, the surface Ni atoms were uniformly isolated by the Zn atoms, leading to a decrease in the ensembles of surface Ni atoms. Moreover, the ensembles are expected to be smaller and smaller with decreasing Ni/Zn atomic ratios.

**Table 1**  
Structural properties of  $\text{Ni}_x\text{Zn}_y\text{Al}$  catalysts.

Ni/Zn atomic ratio	NiZn alloy or IMC phase	Space group (Ni-Zn)	Lattice parameter <sup>a</sup> (nm)	Crystallite size <sup>b</sup> (nm)	$S_{\text{BET}}$ ( $\text{m}^2 \text{ g}^{-1}$ )	$d_p$ (nm)	$V_p$ ( $\text{cm}^3 \text{ g}^{-1}$ )
3/0	Ni	Fm-3m	$a = 0.3521$	5.1	93	14	0.3
50/1	Ni-Zn	Fm-3m	$a = 0.3522$	5.3	—	—	—
8/1	Ni-Zn	Fm-3m	$a = 0.3538$	5.5	102	18	0.4
4/1	Ni-Zn	Fm-3m	$a = 0.3540$	5.7	103	17	0.4
3/1	$\text{Ni}_4\text{Zn}$	Fm-3m	$a = 0.3567$	6.0	101	19	0.5
2/1	$\text{Ni}_{70}\text{Zn}_{30}$	Fm-3m	$a = 0.3582$	6.1	102	22	0.6
1/1	t-NiZn	I4/mmm (139)	$a = 0.2759$ , $b = 0.2759$ , $c = 0.3220$	6.7	81	23	0.5
1/2	t-NiZn	I4/mmm (139)	$a = 0.2803$ , $b = 0.2803$ , $c = 0.3026$	9.0	79	27	0.5
1/8	c-NiZn	Pm-3m(221)	$a = 0.2916$	6.6	110	38	1.0
0/3	—	—	—	—	101	42	1.1

<sup>a</sup> Lattice parameters determined from Rietveld refinement of XRD data.

<sup>b</sup> Calculated by the Scherrer equation.



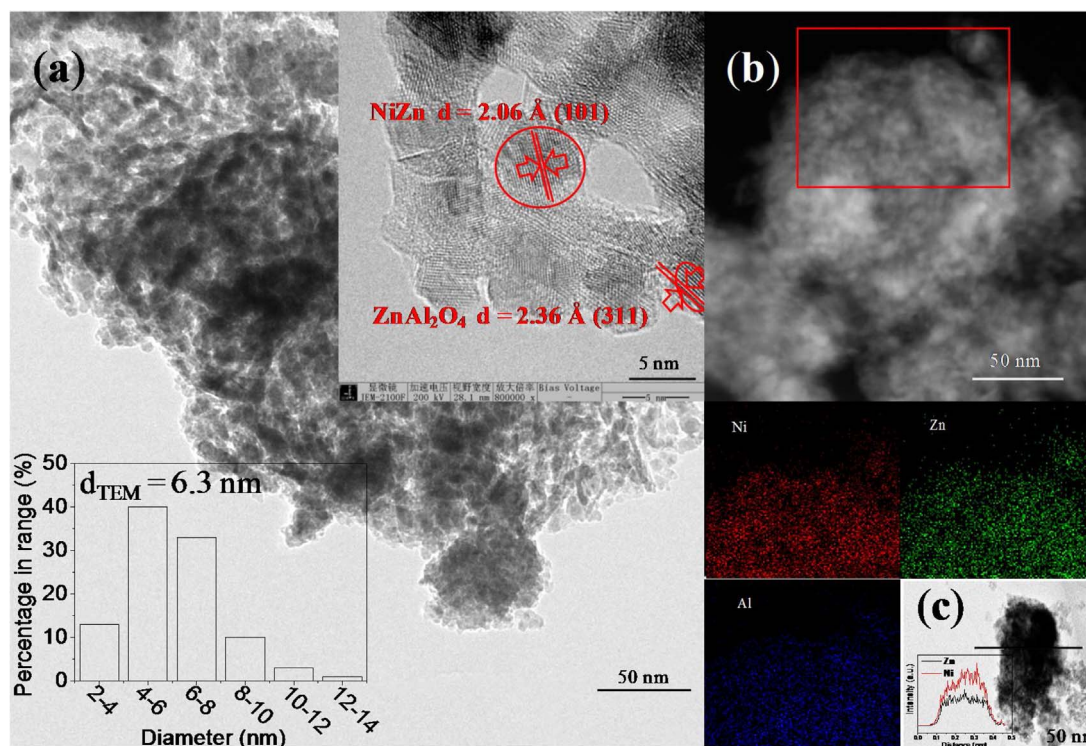


Fig. 3. (a) TEM (insets: HRTEM image and particle size distribution), (b) STEM image and corresponding EDS mapping and (c) STEM image and corresponding EDS line scanning profiles of Ni and Zn element on  $\text{Ni}_1\text{Zn}_1\text{Al}$ .

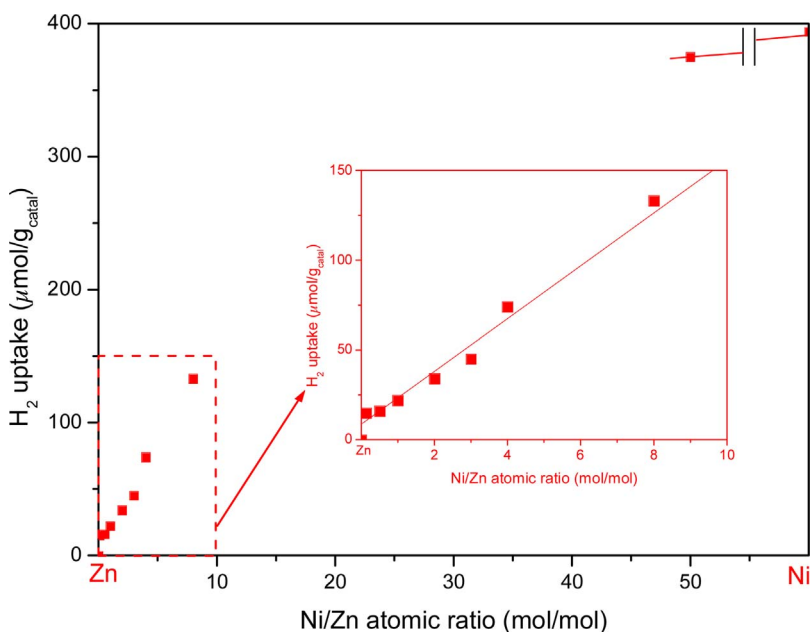


Fig. 4.  $\text{H}_2$  uptakes of  $\text{Ni}_x\text{Zn}_y\text{Al}$  catalysts with different Ni/Zn atomic ratios.

To further confirm the reduced ensembles of Ni sites, the magnetism of  $\text{Ni}_x\text{Zn}_y\text{Al}$  was measured. Fig. 5 shows the magnetic hysteresis loops of  $\text{Ni}_x\text{Zn}_y\text{Al}$  at room temperature. Because the Ni content was different in  $\text{Ni}_x\text{Zn}_y\text{Al}$ , we normalized the magnetization data with respect to per gram Ni.  $\text{Ni}_3\text{Zn}_0\text{Al}$  gave the saturation magnetization of 35.2  $\text{emu/g}_{\text{Ni}}$ , which was much lower than that of bulk metallic Ni with a diameter of 2–3  $\mu\text{m}$  at 27  $^{\circ}\text{C}$  (55  $\text{emu/g}_{\text{Ni}}$ ) [41]. This finding is ascribed to the smaller metallic Ni crystallites (5.1 nm) in  $\text{Ni}_3\text{Zn}_0\text{Al}$  [42,43]. The saturation magnetizations of  $\text{Ni}_8\text{Zn}_1\text{Al}$ ,  $\text{Ni}_4\text{Zn}_1\text{Al}$ ,  $\text{Ni}_2\text{Zn}_1\text{Al}$  and  $\text{Ni}_1\text{Zn}_1\text{Al}$  were 30.5, 26.3, 17.1 and 0.6  $\text{emu/g}_{\text{Ni}}$ , respectively. That is, the saturation magnetization remarkably decreased with the decrease in the

Ni/Zn ratio. It is noteworthy that this finding does not correspond to the increase in the Ni-Zn alloy and IMC crystallite sizes. We suggest that this finding can be interpreted by the dilution effect of Zn atoms because Zn is non-magnetic. In other word, with decreasing Ni/Zn ratios, the average number of contiguous Ni atoms reduces, i.e., the ensembles of Ni atoms isolated by the Zn atoms in the alloys and IMC particles decreased. Particularly,  $\text{Ni}_1\text{Zn}_1\text{Al}$  nearly lost ferromagnetism due to the formation of t-NiZn. This finding is related to the tetragonal  $\text{L1}_0$  structure of t-NiZn, where each Ni atom was coordinated by 8 Zn nearest neighbors and 6 more distant Ni neighbors [37], i.e., each Ni atom is uniformly isolated by the Zn atoms.

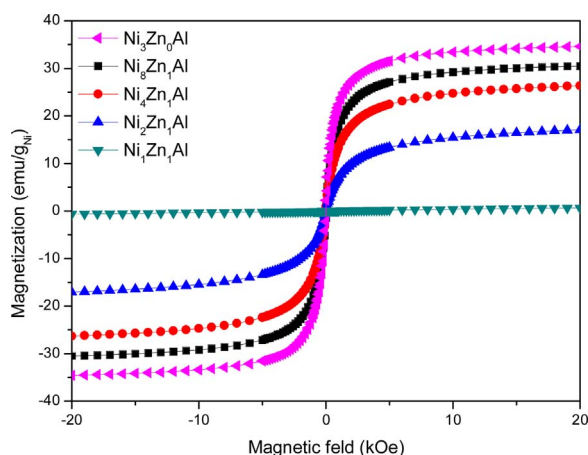


Fig. 5. Magnetic hysteresis loops of some  $\text{Ni}_x\text{Zn}_{3-x}\text{Al}$  samples at 27 °C.

In short, the  $\text{H}_2$  chemisorption and magnetism results indicate that the ensembles of Ni atoms in the bulk/on the surface of alloys and IMCs all tend to decrease with decreasing Ni/Zn ratios.

**3.1.3.3. XPS and CO-TPD.** Taking  $\text{Ni}_3\text{Zn}_0\text{Al}$  and  $\text{Ni}_1\text{Zn}_1\text{Al}$  as examples, XPS was performed to obtain information about the electronic interaction between the Ni and Zn atoms. As shown in Fig. 6, for  $\text{Ni}_3\text{Zn}_0\text{Al}$ , the Ni  $2p_{3/2}$  binding energy (BE) of 853.1 eV and the Ni  $2p_{1/2}$  BE of 870.3 eV are assigned to metallic  $\text{Ni}^0$ , while the Ni  $2p_{3/2}$  BE of 856.7 eV and the Ni  $2p_{1/2}$  BE of 873.8 eV are attributed to  $\text{Ni}^{2+}$  species [44], which is related to the catalyst passivation and/or the unreduced nickel species. Clearly, metallic  $\text{Ni}^0$  species were dominating on  $\text{Ni}_3\text{Zn}_0\text{Al}$ . Compared with  $\text{Ni}_3\text{Zn}_0\text{Al}$ ,  $\text{Ni}_1\text{Zn}_1\text{Al}$  showed slightly larger Ni  $2p_{3/2}$  and  $2p_{1/2}$  BEs (853.2 and 870.7 eV, respectively) due to metallic  $\text{Ni}^0$ , revealing a charge transfer from the Ni atoms to the Zn atoms. The existence of metallic  $\text{Zn}^0$  is confirmed by the Zn  $\text{L}_{3\text{M}_{45}\text{M}_{45}}$  Auger spectrum with a kinetic energy of 991.7 eV [45,46] (Fig. S7). The 2p and valence electron transfer from Ni toward Zn has been reported for Ni-Zn alloys [26,47]. Given that the difference in the Ni 2p BEs due to metallic  $\text{Ni}^0$  was very small between  $\text{Ni}_3\text{Zn}_0\text{Al}$  and  $\text{Ni}_1\text{Zn}_1\text{Al}$ , we also adopted CO-TPD to further investigate the electronic interaction between Ni and Zn in Ni-Zn alloys and IMCs.

It has been well-demonstrated that CO adsorption strength is related to the electronic properties of the transition metal (the expatiation is shown in Supplementary information) [26,48–51], and a high correlation between the CO desorption temperature and the electron density

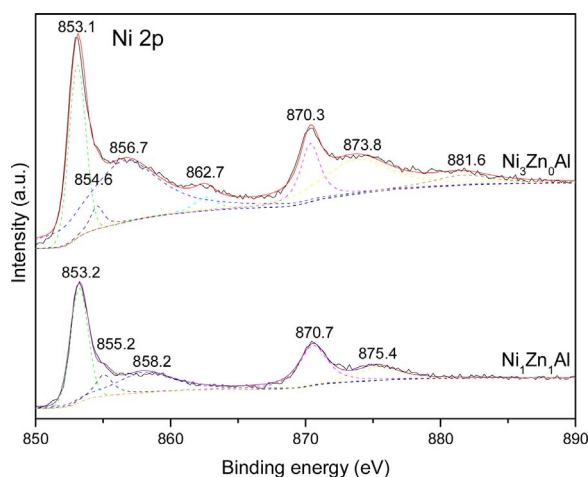


Fig. 6. Ni 2p XPS spectra of  $\text{Ni}_3\text{Zn}_0\text{Al}$  and  $\text{Ni}_1\text{Zn}_1\text{Al}$ .

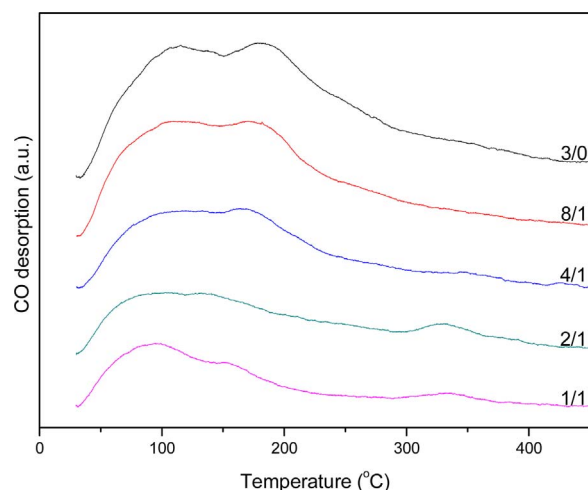


Fig. 7. CO-TPD profiles of different  $\text{Ni}_x\text{Zn}_{3-x}\text{Al}$  catalysts.

Note: the number on the curve indicates the Ni/Zn atomic ratio.

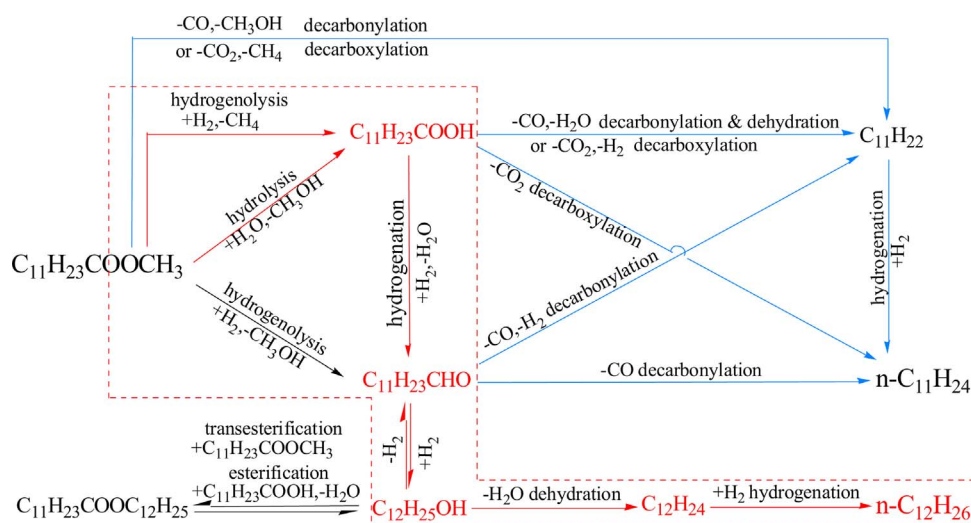
has been established [51,52]. The larger the electron density of the metal atoms, the higher the CO desorption temperature.

Compared to metallic Ni that can strongly adsorb CO, metallic Zn has very weak CO adsorption [53]. For the Ni-Zn alloy, the Ni atoms contribute to adsorbing CO, while CO adsorption on the Zn atoms can be ignored [26]. Fig. 7 shows the CO-TPD profiles of  $\text{Ni}_x\text{Zn}_{3-x}\text{Al}$  samples.  $\text{Ni}_3\text{Zn}_0\text{Al}$  produced two desorption peaks at 115 and 179 °C. In contrast, the presence of Zn led to a shift in the desorption peaks to low temperatures, which is more obvious with decreasing Ni/Zn ratios. It is noteworthy that, compared with that at low temperature, the peak area at high temperature decreased more remarkably as the Ni/Zn ratio decreased. This finding also means that the strongly adsorbed CO species were more obviously suppressed. In short, the CO adsorption strength was reduced due to the formation of Ni-Zn alloys and IMCs, and the higher the proportion of Zn in the alloys and IMCs, the weaker the CO adsorption on metallic Ni sites. This finding is ascribed to the  $d$  electron transfer from Ni to the region around the Ni-Zn bonds, leading to the decrease in the available electrons for  $\pi$  back-donation to CO, and subsequently the adsorption of CO was weakened [26].

Given the XPS and CO-TPD results and the result reported in the literature [26], we conclude that there is a charge transfer from Ni to Zn in the Ni-Zn alloys and IMCs, which becomes increasingly remarkable as the Ni/Zn ratio decreases.

### 3.2. Catalyst performance

The performance of  $\text{Ni}_x\text{Zn}_{3-x}\text{Al}$  catalysts for the deoxygenation of methyl laurate was mainly tested at 330 and 400 °C. Here, the target deoxygenated products were  $\text{C}_{11}$  and  $\text{C}_{12}$  hydrocarbons, which are produced from the decarbonylation/decarboxylation and HDO pathways, respectively. However, the undesirable  $\text{C}_1 \sim \text{C}_5$  and  $\text{C}_6 \sim \text{C}_{10}$  hydrocarbons, generated from the C–C bond hydrogenolysis, were found in gaseous and liquid effluents, respectively. Particularly,  $\text{CH}_4$  can also be derived from methanation of  $\text{CO}/\text{CO}_2$ . To suppress C–C bond hydrogenolysis and methanation is one of aims of the present work. Additionally,  $\text{C}_{12}$  oxygenated intermediates (denoted as  $\text{oxyC}_{12}$ , including lauryl alcohol, lauric acid, lauraldehyde and lauryl laurate) were detected in the liquid effluent, and they are produced via a sequential reaction, i.e., methyl laurate  $\rightarrow$  lauric acid  $\rightarrow$  lauraldehyde  $\rightarrow$  lauryl alcohol  $\rightarrow$   $\text{C}_{12}$  hydrocarbons, which has been confirmed by testing various oxygen moieties (e.g., lauric acid, lauraldehyde and lauryl alcohol) in our previous work [10]. Lauryl laurate can be generated from the esterification of lauryl alcohol and lauric acid and/or the interesterification between lauryl alcohol and methyl laurate.



Combining these findings with the reports in the literature [10,54,55], the deoxygenation pathway of methyl laurate is proposed in Scheme 1.

### 3.2.1. Catalyst performance at 330 °C

As shown in Fig. 8(a), on the whole, the introduction of Zn reduced the conversion of methyl laurate. However, the conversion did not always decrease with decreasing Ni/Zn ratios. Methyl laurate was almost completely converted on  $\text{Ni}_3\text{Zn}_0\text{Al}$  and  $\text{Ni}_{50}\text{Zn}_1\text{Al}$  at 330 °C. Its conversion decreased to 50.9% with decreasing Ni/Zn ratios to 4/1. However, as the Ni/Zn ratio further decreased, the conversion increased and reached a maximum (79.5%) at a Ni/Zn ratio of 1/1.  $\text{Ni}_1\text{Zn}_2\text{Al}$  had slightly lower conversion (76.6%) than  $\text{Ni}_1\text{Zn}_1\text{Al}$ . Clearly, there was a volcano-type change (i.e., first increase and then decrease) in the conversion at Ni/Zn atomic ratios between 4/1 and 1/8. Additionally,  $\text{Ni}_0\text{Zn}_3\text{Al}$  had the lowest conversion of 15.5%. We found that the conversion of methyl laurate was only 0.5% on  $\gamma$ -alumina at 330 °C. Therefore, the main active component in  $\text{Ni}_x\text{Zn}_y\text{Al}$  was metallic Ni. This finding is related to the decrease in the Ni content, and consequently the decrease in the surface Ni site density (Fig. 4). To obtain the intrinsic reactivity of per surface Ni site, the TOFs of methyl laurate on different catalysts were calculated (Fig. 8(b)). Interestingly, different from the case in the conversion, TOFs on  $\text{Ni}_3\text{Zn}_0\text{Al}$  and  $\text{Ni}_{50}\text{Zn}_1\text{Al}$  were lower than those of other catalysts. TOFs were lower than  $1.2 \text{ s}^{-1}$  on  $\text{Ni}_x\text{Zn}_y\text{Al}$  with Ni/Zn ratios  $\geq 2/1$ , while they were larger than  $2.7 \text{ s}^{-1}$  at Ni/Zn ratios between 1/1 and 1/8.  $\text{Ni}_1\text{Zn}_2\text{Al}$  had the highest TOF ( $4.1 \text{ s}^{-1}$ ), followed by  $\text{Ni}_1\text{Zn}_1\text{Al}$  ( $3.2 \text{ s}^{-1}$ ). Therefore, a suitable amount of Zn (Ni/Zn ratio  $< 2/1$ ) remarkably enhanced the TOFs. This finding indicates a synergistic effect between Ni and Zn for the conversion of methyl laurate (discussed in Section 4.2). This synergistic effect can also account for the volcano-type change of the conversion at Ni/Zn ratios between 4/1 and 1/8.

Fig. 9(a) shows the total selectivity to  $\text{C}_{11}$  and  $\text{C}_{12}$  hydrocarbons (denoted as  $S_{\text{C}_{11}+\text{C}_{12}}$ ). It is necessary to note that, apart from  $n$ -undecane ( $n\text{-C}_{11}$ ) and  $n$ -dodecane ( $n\text{-C}_{12}$ ), there is only a small amount of other  $\text{C}_{11}$  and  $\text{C}_{12}$  hydrocarbons (including undecene, dodecene and isomeric  $\text{C}_{11}$  and  $\text{C}_{12}$ ) with total selectivity less than 2%. The formation of alkenes with different isomers has also reported by Hocevar et al. [56].  $S_{\text{C}_{11}+\text{C}_{12}}$  on  $\text{Ni}_3\text{Zn}_0\text{Al}$  was only 12.3%. With the decrease in the Ni/Zn ratio, it increased to the maximum (93.1%) on  $\text{Ni}_8\text{Zn}_1\text{Al}$  and then quickly decreased. As presented in Fig. 9(b), the selectivity to oxy $\text{C}_{12}$  (denoted as  $S_{\text{oxy}}$ ) on  $\text{Ni}_3\text{Zn}_0\text{Al}$  was close to zero.  $\text{Ni}_{50}\text{Zn}_1\text{Al}$  and  $\text{Ni}_8\text{Zn}_1\text{Al}$  had slightly higher  $S_{\text{oxy}}$  (0.6% and 2.3%, respectively) compared to  $\text{Ni}_3\text{Zn}_0\text{Al}$ . As the Ni/Zn ratio further decreased,  $S_{\text{oxy}}$  rapidly increased and reached a maximum (70.0%) on  $\text{Ni}_1\text{Zn}_2\text{Al}$ . The main oxygenated intermediates were lauryl alcohol and lauryl laurate as

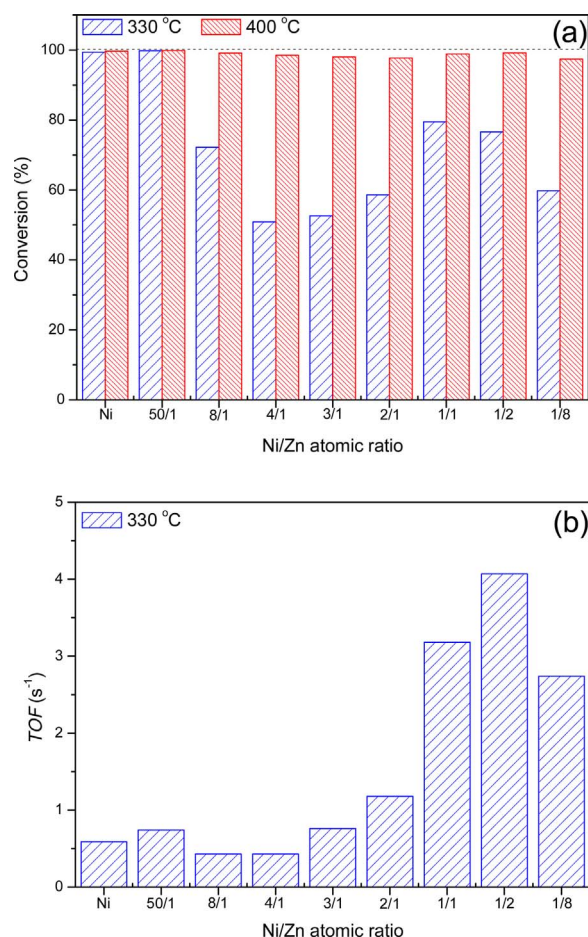


Fig. 8. Deoxygenation of methyl laurate on different  $\text{Ni}_x\text{Zn}_y\text{Al}$  catalysts. (a) Conversion of methyl laurate at 330 and 400 °C; (b) Turnover frequency of methyl laurate at 330 °C.

shown in Fig. S8. For instance, as shown in Table S4 in Supplementary information, the selectivities to lauryl alcohol and lauryl laurate on  $\text{Ni}_1\text{Zn}_2\text{Al}$  were 53.4% and 13.9%, respectively; low selectivity to lauraldehyde (2.5%) is ascribed to its high reactivity, which can be easily hydrogenated to lauryl alcohol and/or polymerized to heavy products [10]. Additionally, the selectivity to laurate acid was also very low ( $\sim 0.2\%$ ), which is attributed to the fact that it can easily react with



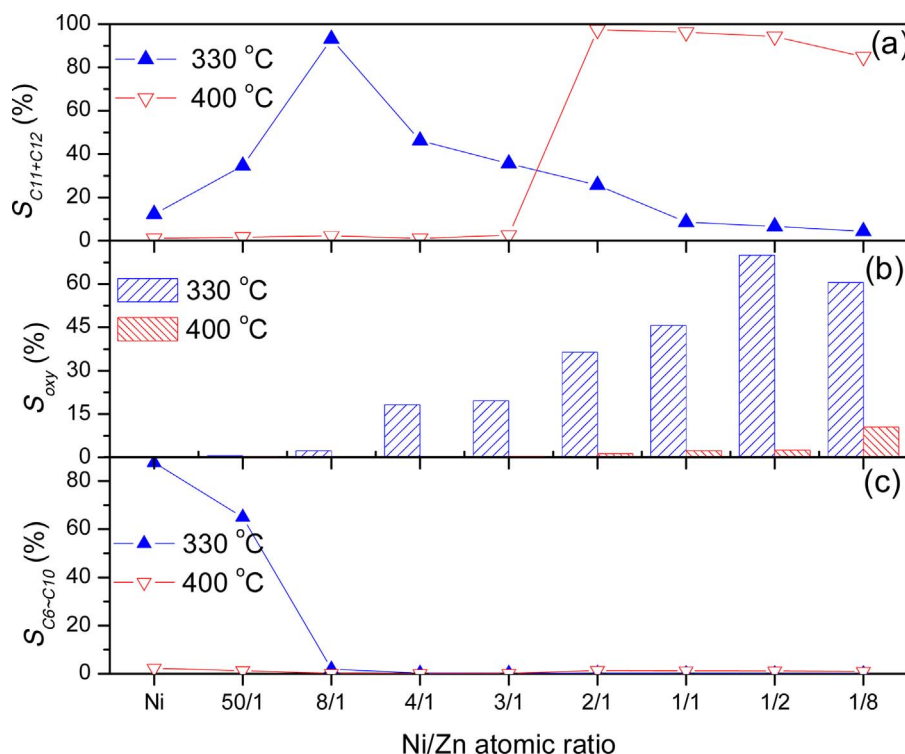


Fig. 9. Product selectivity on different  $\text{Ni}_x\text{Zn}_y\text{Al}$  catalysts. (a) Total selectivity to  $\text{C}_{11}$  and  $\text{C}_{12}$  hydrocarbons; (b) selectivity to oxygenated intermediates; and (c) selectivity to cracking products ( $\text{C}_6 \sim \text{C}_{10}$ ).

lauryl alcohol to form lauryl laurate. Correlated with the  $\text{C}_{11}/(\text{C}_{12} + \text{oxyC}_{12})$  molar ratio indicated in Fig. 10, the formation of the Ni-Zn alloys and IMCs promoted the HDO pathway, producing more  $\text{oxyC}_{12}$  intermediates. However, with decreasing Ni/Zn ratios, the increase in  $S_{\text{oxy}}$  indicates that the catalyst reactivity for the deoxygenation was reduced, which is also attributed to the decrease in surface Ni site density.

As mentioned above, methyl laurate was completely converted on  $\text{Ni}_3\text{Zn}_0\text{Al}$ , while the sum of  $S_{\text{C11+C12}}$  and  $S_{\text{oxy}}$  was only 12.3% (Fig. S9). Such a surprising result is consistent with high selectivity to  $\text{C}_6 \sim \text{C}_{10}$  hydrocarbons ( $S_{\text{C6-C10}}$ , 87.7%) on  $\text{Ni}_3\text{Zn}_0\text{Al}$  (Fig. 9(c)), indicative of high reactivity of metallic Ni for C–C bond hydrogenolysis. The high reactivity of  $\text{Ni}_3\text{Zn}_0\text{Al}$  for C–C bond hydrogenolysis was further confirmed by the complete conversion of  $n\text{-C}_{12}$  as the reactant (Table S5). In contrast,  $\text{Ni}_{50}\text{Zn}_1\text{Al}$  had a lower  $S_{\text{C6-C10}}$  (65.0%) than  $\text{Ni}_3\text{Zn}_0\text{Al}$ . It is noteworthy that  $S_{\text{C6-C10}}$  was as low as 0.2% on  $\text{Ni}_x\text{Zn}_y\text{Al}$ , with Ni/Zn ratios  $\leq 8/1$ . Obviously, the formation of Ni-Zn alloys and IMCs remarkably suppressed C–C bond hydrogenolysis, which was also confirmed by the only  $\sim 1\%$  conversion of  $n\text{-C}_{12}$  as the reactant on  $\text{Ni}_1\text{Zn}_1\text{Al}$  (Table S5).

Given that the selectivities in Fig. 9 were obtained at different conversions of methyl laurate on different catalysts, we also evaluated different catalysts to give similar conversions through changing the WHSV of methyl laurate to reasonably compare the selectivities. As indicated in Table S6 in the Supplementary information, at a similar conversion of  $76 \pm 4\%$  at 330 °C, with decreasing Ni/Zn ratios,  $S_{\text{C11+C12}}$  first increased and then decreased, and  $S_{\text{oxy}}$  and  $S_{\text{C6-C10}}$  tended to increase and decrease, respectively. Clearly, the change tendency of the product selectivity with decreasing Ni/Zn ratios in Table S6 is the same as that presented in Fig. 9. Additionally, we also calculated TOFs on different catalysts with similar conversions ( $76 \pm 4\%$ ) (Table S6), and the change tendencies for TOFs with decreasing Ni/Zn ratios is also the same as that presented in Fig. 8(b) with decreasing Ni/Zn ratios.

Here, although the C–C bond hydrogenolysis occurred, the  $\text{C}_{11}/(\text{C}_{12} + \text{oxyC}_{12})$  ratio can approximately denote the selectivity between the decarbonylation/decarboxylation and HDO pathways. As shown in

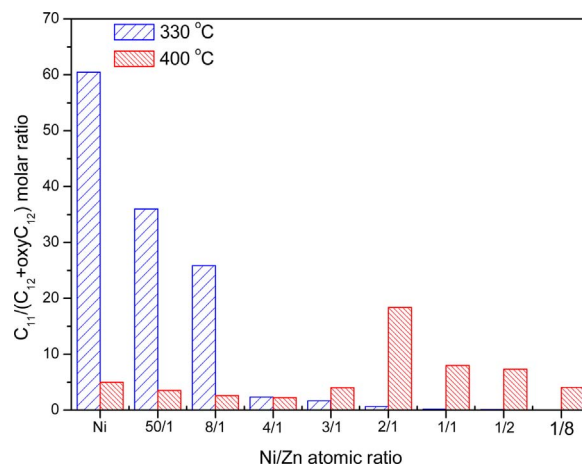


Fig. 10.  $\text{C}_{11}/(\text{C}_{12} + \text{oxyC}_{12})$  molar ratios on different  $\text{Ni}_x\text{Zn}_y\text{Al}$  catalysts at 330 and 400 °C.

Fig. 10, the  $\text{C}_{11}/(\text{C}_{12} + \text{oxyC}_{12})$  ratio reached 60.5 on  $\text{Ni}_3\text{Zn}_0\text{Al}$ , that is, the decarbonylation/decarboxylation pathway dominated.  $\text{Ni}_{50}\text{Zn}_1\text{Al}$  and  $\text{Ni}_8\text{Zn}_1\text{Al}$  also produced high  $\text{C}_{11}/(\text{C}_{12} + \text{oxyC}_{12})$  ratios (36.0 and 25.9, respectively), but they were lower than that on  $\text{Ni}_3\text{Zn}_0\text{Al}$ . Amazingly, the  $\text{C}_{11}/(\text{C}_{12} + \text{oxyC}_{12})$  ratio was only 2.3 on  $\text{Ni}_4\text{Zn}_1\text{Al}$  and close to zero with the further decrease in the Ni/Zn ratio to 2/1. Clearly, the decarbonylation/decarboxylation pathway was remarkably suppressed due to the formation of Ni-Zn alloys and IMCs, while the HDO pathway was promoted. This finding is more obvious at the Ni/Zn ratios  $< 4/1$ . It is necessary to note that Ni-Zn IMCs formed when the Ni/Zn ratios were between 1/1 and 1/8.

The  $(\text{CO} + \text{CO}_2)/\text{C}_{11}$  molar ratio is used to describe methanation reactivity. The  $\text{C}_{11}$  hydrocarbons are derived from the decarbonylation/decarboxylation of methyl laurate and its oxygenated intermediates (Scheme 1) [10]. The  $(\text{CO} + \text{CO}_2)/\text{C}_{11}$  molar ratio should be 1.0 if no methanation and C–C bond hydrogenolysis occurred. As shown in Fig. 11, the  $(\text{CO} + \text{CO}_2)/\text{C}_{11}$  molar ratio was zero on  $\text{Ni}_3\text{Zn}_0\text{Al}$  and



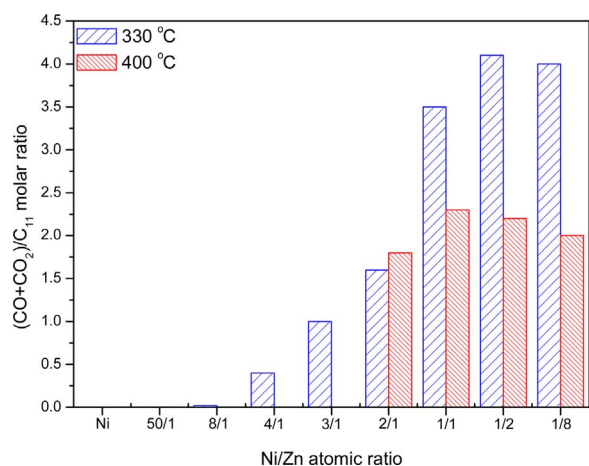


Fig. 11. (CO + CO<sub>2</sub>)/C<sub>11</sub> molar ratios on different Ni<sub>x</sub>Zn<sub>y</sub>Al catalysts at 330 and 400 °C.

Ni<sub>50</sub>Zn<sub>1</sub>Al, where decarbonylation/decarboxylation dominated, indicating that CO and CO<sub>2</sub> were completely hydrogenated to CH<sub>4</sub>. To confirm this, the methanation of CO was tested on Ni<sub>3</sub>Zn<sub>0</sub>Al, and it was found that CO was completely converted into CH<sub>4</sub> even at 330 °C (Table 2). With decreasing Ni/Zn ratios, the (CO + CO<sub>2</sub>)/C<sub>11</sub> molar ratio increased. Ni<sub>8</sub>Zn<sub>1</sub>Al produced a (CO + CO<sub>2</sub>)/C<sub>11</sub> ratio of 0.02. When the Ni/Zn ratio was less than 3/1, the (CO + CO<sub>2</sub>)/C<sub>11</sub> ratio was even larger than 1.0. Particularly, it reached ~ 4.0 on Ni<sub>1</sub>Zn<sub>2</sub>Al and Ni<sub>1</sub>Zn<sub>8</sub>Al. Such high (CO + CO<sub>2</sub>)/C<sub>11</sub> molar ratios are probably ascribed to the following reasons: 1) C–C bond hydrogenolysis consumed some C<sub>11</sub> hydrocarbon, and 2) the hydrogenolysis or hydrolysis of the C–OCH<sub>3</sub> bond in methyl laurate produced methanol, followed by the decomposition to CO. We also found that no methanation of CO occurred on Ni<sub>1</sub>Zn<sub>1</sub>Al at 330 °C (Table 2). Therefore, methanation was efficiently suppressed due to the formation of the Ni–Zn alloys and IMCs, especially the formation of IMCs.

From the above, the formation of Ni–Zn alloys and IMCs (especially the latter) in Ni<sub>x</sub>Zn<sub>y</sub>Al promoted the HDO pathway while suppressing C–C bond hydrogenolysis and methanation.

From the viewpoint of thermodynamics, increasing temperature will promote decarbonylation/decarboxylation and C–C bond hydrogenolysis [2]. At 330 °C, Ni-rich Ni<sub>8</sub>Zn<sub>1</sub>Al had higher reactivity for decarbonylation/decarboxylation and C–C bond hydrogenolysis than Ni<sub>1</sub>Zn<sub>1</sub>Al. Selecting these two catalysts, we tested the effect of reaction temperature (330, 350, 380 and 400 °C) on their reactivities for the deoxygenation of methyl laurate. As shown in Table S7 in Supplementary information, for Ni<sub>1</sub>Zn<sub>1</sub>Al, with increasing reaction temperatures from 330 to 400 °C, the conversion of methyl laurate and  $S_{C11+C12}$  increased from 79.5% to 98.9% and from 8.6% to 96.2%, respectively, while the  $S_{oxy}$  and (CO + CO<sub>2</sub>)/C<sub>11</sub> molar ratio decreased from 45.7% to 2.3% and from 3.5 to 1.9, respectively. It is interesting that the (CO + CO<sub>2</sub>)/C<sub>11</sub> molar ratio was still larger than 1.0, and there was a very high  $S_{C11+C12}$  at 400 °C, indicative of very low reactivity of Ni<sub>1</sub>Zn<sub>1</sub>Al for methanation and C–C bond hydrogenolysis. However, for Ni<sub>8</sub>Zn<sub>1</sub>Al (Table S8), although the conversion increased from 72.2% to 99.1% and  $S_{oxy}$  decreased from 2.3% to 0.1% with increasing temperatures

from 330 to 400 °C,  $S_{C11+C12}$  remarkably decreased from 93.1% to 2.3% due to serious C–C bond hydrogenolysis. Moreover, the (CO + CO<sub>2</sub>)/C<sub>11</sub> molar ratio was always close to or equal to 0 between 330 and 400 °C, indicative of a complete methanation of CO and CO<sub>2</sub>. Clearly, the Ni-rich catalysts exhibited different reactivity for C–C bond hydrogenolysis and CO methanation from the catalysts with high levels of Zn, especially at high reaction temperatures. To further verify the effect of Zn on the catalyst reactivity (especially for C–C bond hydrogenolysis and CO methanation), we focused on the performance of all catalysts at a harsher temperature (i.e., 400 °C).

### 3.2.2. Catalyst performance at 400 °C

At 400 °C, the conversion of methyl laurate was close to 100% on the catalysts (Fig. 8 (a)).  $S_{C11+C12}$  was close to zero on the catalysts with the Ni/Zn ratio  $\geq 3/1$  (Fig. 9 (a)). Moreover, the total selectivity to C<sub>11</sub> ~ C<sub>12</sub> hydrocarbons and oxyC<sub>12</sub> on the catalysts was very low (~ 3.1%) (Fig. S9), while a large amount of CH<sub>4</sub> was detected in the gaseous effluent (C<sub>1</sub>/C<sub>1-5</sub> molar ratio  $\geq 96.6$ ), indicative of more serious C–C bond hydrogenolysis at 400 °C. Surprisingly,  $S_{C11+C12}$  reached as high as 97.4% and 96.2% when the Ni/Zn atomic ratio was 2/1 and 1/1, respectively. As the Ni/Zn ratio further decreased to 1/8,  $S_{C11+C12}$  slowly decreased to 84.9% (Fig. 9(a)), while  $S_{oxy}$  increased to 10.5% (Fig. 9(b)). Clearly, the formation of Ni–Zn IMCs at Ni/Zn ratios  $\leq 2/1$  is very necessary for remarkably suppressing C–C bond hydrogenolysis.

Because the main product was CH<sub>4</sub> on the catalysts with the Ni/Zn ratios  $\geq 3/1$ , the C<sub>11</sub>/(C<sub>12</sub> + oxyC<sub>12</sub>) molar ratios on these catalysts cannot provide true information about the deoxygenation pathways (Fig. 10). When the Ni/Zn ratio was  $\leq 2/1$ , the C<sub>11</sub>/(C<sub>12</sub> + oxyC<sub>12</sub>) molar ratios decreased with decreasing Ni/Zn ratios, which is also indicative of the promotional effect of Zn on the HDO pathway. However, the C<sub>11</sub>/(C<sub>12</sub> + oxyC<sub>12</sub>) molar ratios were much higher at 400 °C than at 330 °C, i.e., the increase in temperature greatly promoted endothermic decarbonylation/decarboxylation.

Additionally, no CO and CO<sub>2</sub> were detected on the catalysts with Ni/Zn ratios  $\geq 3/1$ . For the catalysts with Ni/Zn ratios  $\leq 2/1$ , the (CO + CO<sub>2</sub>)/C<sub>11</sub> molar ratios were larger than 1.0 (Fig. 11), even exceeding 2.0 on Ni<sub>1</sub>Zn<sub>1</sub>Al and Ni<sub>1</sub>Zn<sub>2</sub>Al. The (CO + CO<sub>2</sub>)/C<sub>11</sub> molar ratios were lower at 400 °C than at 330 °C. This finding is related to the fact that the increasing temperature promoted the methanation of CO. As shown in Table 2, 7.2% CO was converted into CH<sub>4</sub> on Ni<sub>1</sub>Zn<sub>1</sub>Al at 400 °C. This finding also indicates that t-NiZn IMC in Ni<sub>1</sub>Zn<sub>1</sub>Al was very lowly reactive for methanation even at 400 °C.

To sum up, the formation of Ni–Zn alloys and IMCs promoted the HDO pathway and suppressed decarbonylation/decarboxylation reactions, C–C bond hydrogenolysis and methanation, especially with the formation of Ni–Zn IMCs. This finding is more obviously reflected by performance at 400 °C.

## 4. Discussion

Here, the supported Ni–Zn alloys and IMCs were prepared from LDH precursors, and their structure depended on the Ni/Zn ratios. The Ni-rich alloys were generated in Ni<sub>x</sub>Zn<sub>y</sub>Al with Ni/Zn ratios between 50/1 and 3/1, while t-NiZn IMCs were synthesized at Ni/Zn ratios of 1/1 and 1/2, and c-NiZn IMCs formed at a Ni/Zn ratio of 1/8. In contrast with the Ni-rich alloys which were formed by random substitution of Zn in the lattice of fcc metallic Ni, t-NiZn and c-NiZn IMCs possess tetragonal and cubic structures [37], respectively. Given the structural properties of IMCs [14,57], Ni and Zn are expected to more homogeneously distribute in t-NiZn and c-NiZn than in Ni-rich alloys. The HAADF-STEM-EDS mappings demonstrate a homogenous distribution of Ni and Zn in Ni<sub>1</sub>Zn<sub>1</sub>Al. From the H<sub>2</sub> chemisorption and magnetization results, the ensembles of Ni sites in/on the crystallites became smaller and smaller with decreasing Ni/Zn ratios. Additionally, there was a small charge transfer from Ni to Zn as revealed by XPS and CO-TPD, and the amount

Table 2  
CO hydrogenation on Ni<sub>3</sub>Zn<sub>0</sub>Al and Ni<sub>1</sub>Zn<sub>1</sub>Al.<sup>a</sup>

Catalyst	Reactants	Molar ratio of gaseous components in product	
		330 °C	400 °C
Ni <sub>3</sub> Zn <sub>0</sub> Al	CO + H <sub>2</sub>	CH <sub>4</sub> :CO = 1:0	CH <sub>4</sub> :CO <sub>2</sub> :CO = 1:0:0
Ni <sub>1</sub> Zn <sub>1</sub> Al	CO + H <sub>2</sub>	CH <sub>4</sub> :CO = 0:1	CH <sub>4</sub> :CO <sub>2</sub> :CO = 0.084:0.074:1

<sup>a</sup> Reaction conditions: 3.0 MPa, H<sub>2</sub>/CO molar ratio = 25, gaseous hourly space velocity 7.31 × 10<sup>3</sup> ml<sub>gatal</sub><sup>-1</sup> h<sup>-1</sup>.

of charge transfer tended to increase with decreasing Ni/Zn ratios. In brief, Zn geometrically and electronically modified metallic Ni in Ni-Zn alloys and IMCs.

As indicated in Section 3.2 in the deoxygenation of methyl laurate, although the formation of Ni-Zn alloys and IMCs reduced catalyst reactivity for deoxygenation because of the decrease in nickel content and thus surface Ni atom density, it suppressed C–C bond hydrogenolysis and methanation, especially the formation of t- and c-NiZn. Additionally, the presence of Zn promoted the HDO pathway. The performance of Ni-Zn alloys and IMCs is closely associated with the geometric and electronic modification of Zn on Ni.

#### 4.1. Catalytic reactivity

Because the conversions of methyl laurate were close to or equal to 100% at 400 °C on  $\text{Ni}_x\text{Zn}_y\text{Al}$  catalysts, the effect of Zn on catalyst reactivity was analyzed on the base of the conversions at 330 °C. As illustrated in Fig. 8(a), at 330 °C, the conversions of methyl laurate were 100% on  $\text{Ni}_3\text{Zn}_0\text{Al}$  and  $\text{Ni}_{50}\text{Zn}_{1}\text{Al}$ . With decreasing Ni/Zn ratios, the conversion first decreased to 50.9% at a Ni/Zn ratio of 4/1 and then increased to a maximum (79.5%) at a Ni/Zn ratio of 1/1. This finding does not correspond to the decreased trend in  $\text{H}_2$  uptake. For this case, we provide the following explanations. First, with decreasing Ni/Zn ratios from 3/0 to 4/1, the conversion decreased, corresponding to the decrease in the  $\text{H}_2$  uptake. This finding is due to that the surface Ni atoms were main active sites because the decarbonylation/decarboxylation pathway dominated with  $\text{C}_{11}/(\text{C}_{12} + \text{oxyC}_{12})$  ratios as high as  $\geq 2.3$  (Fig. 10). Second, with decrease in the Ni/Zn ratio from 3/1 to 1/8, the  $\text{H}_2$  uptake decreased as well. However, the conversion of methyl laurate reached a maximum (79.5%) at the Ni/Zn ratio of 1/1. We considered that the surface Zn atoms on the alloy and IMC particles were not simple spectators and participated in the conversion of methyl laurate. Indeed, the HDO pathway was greatly promoted with decreasing Ni/Zn ratios (Fig. 10). The  $\text{C}_{11}/(\text{C}_{12} + \text{oxyC}_{12})$  ratio was even close to zero at 330 °C when the Ni/Zn ratio was  $\leq 1/1$ . As discussed in the next section, the surface Zn atoms play an essential role in the HDO pathway, and the surface Zn and Ni atoms might cooperatively promote the conversion of methyl laurate. This finding is also supported by the much higher TOFs of methyl laurate on the catalysts with the Ni/Zn ratios of 1/1 and 1/8 than that on  $\text{Ni}_3\text{Zn}_0\text{Al}$  (Fig. 8(b)). Additionally, apart from Ni-Zn alloys and IMCs, ZnO and  $\text{ZnAl}_2\text{O}_4$  phases (especially ZnO) existed in  $\text{Ni}_1\text{Zn}_1\text{Al}$ ,  $\text{Ni}_1\text{Zn}_2\text{Al}$  and  $\text{Ni}_1\text{Zn}_8\text{Al}$  (Fig. 2), and they might contribute to the conversion of methyl laurate.  $\text{Ni}_0\text{Zn}_3\text{Al}$ , which only contained ZnO and  $\text{ZnAl}_2\text{O}_4$  phases, also gave a conversion of 15.5% at 330 °C. Indeed, ZnO and  $\text{ZnAl}_2\text{O}_4$  have been found to be reactive for hydrolysis and transesterification reactions [58,59]. Finally, compared with those on  $\text{Ni}_1\text{Zn}_1\text{Al}$  and  $\text{Ni}_1\text{Zn}_2\text{Al}$ , the lower conversion of methyl laurate on  $\text{Ni}_1\text{Zn}_8\text{Al}$  was ascribed to its many fewer surface Ni sites.

As indicated by  $S_{\text{C}_{11}+\text{C}_{12}}$ ,  $S_{\text{C}_6-\text{C}_{10}}$  and  $S_{\text{oxy}}$ , the formation of Ni-Zn alloys and IMCs also reduced deoxygenation. Compared with  $\text{Ni}_8\text{Zn}_1\text{Al}$ , at 330 °C,  $\text{Ni}_3\text{Zn}_0\text{Al}$  and  $\text{Ni}_{50}\text{Zn}_1\text{Al}$  produced much lower  $S_{\text{C}_{11}+\text{C}_{12}}$  due to their higher reactivity for C–C bond hydrogenolysis, leading to the further conversion of  $\text{C}_{11}$  and  $\text{C}_{12}$  hydrocarbons to lighter ones. Additionally, they had much lower  $S_{\text{oxy}}$  ( $< 0.6\%$ ). That is,  $\text{Ni}_3\text{Zn}_0\text{Al}$  and  $\text{Ni}_{50}\text{Zn}_1\text{Al}$  had higher deoxygenation reactivities than  $\text{Ni}_8\text{Zn}_1\text{Al}$ . When the Ni/Zn ratio was  $\leq 8/1$  and as the Ni/Zn ratio decreased,  $S_{\text{C}_{11}+\text{C}_{12}}$

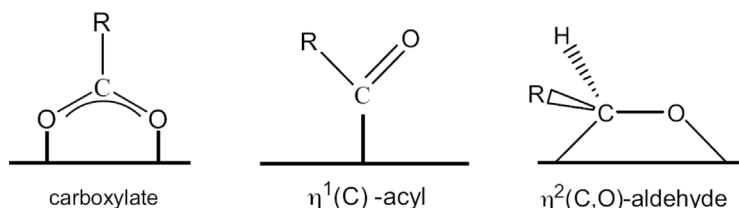
tended to decrease (Fig. 9(a)), while  $S_{\text{oxy}}$  tended to increase (Fig. 9(b)). The site time yield (STY), denoting the amount of  $\text{C}_{11}$  and  $\text{C}_{12}$  hydrocarbons generated per Ni site per second (Fig. S10), further reflected that the deoxygenation ability of the catalysts was reduced by the formation of Ni-Zn alloys and IMCs. This finding should be ascribed to the decreased Ni content with decreasing Ni/Zn ratios. The increasing reaction temperature is an approach to enhancing the deoxygenation reactivity of Ni-Zn alloys and IMCs (Figs. 8 (a) and 9 (a)). For instance, the conversion exceeded 97.7% and  $S_{\text{C}_{11}+\text{C}_{12}}$  reached above 94.3% on  $\text{Ni}_x\text{Zn}_y\text{Al}$  with Ni/Zn ratios between 2/1 and 1/2 at 400 °C.

#### 4.2. Deoxygenation pathway

Because C–C bond hydrogenolysis was very serious on the catalysts with Ni/Zn ratios  $\geq 3/1$  at 400 °C, the effect of Zn on the deoxygenation pathway was also analyzed with data at 330 °C. As shown in Fig. 10, decarbonylation/decarboxylation dominated  $\text{Ni}_3\text{Zn}_0\text{Al}$ , where the  $\text{C}_{11}/(\text{C}_{12} + \text{oxyC}_{12})$  ratio was as high as 60.5, although C–C bond hydrogenolysis also occurred. The introduction of Zn reduced the  $\text{C}_{11}/(\text{C}_{12} + \text{oxyC}_{12})$  ratio, which is more obvious with decreasing Ni/Zn ratios. This finding should be attributed to the formation of the Ni-Zn alloys and IMCs. In the Ni-Zn alloys and IMCs, the Ni atoms were isolated, the ensembles of Ni atoms were reduced, and the electron density of Ni sites was decreased. Moreover, Zn is more oxophilic than Ni [21]. All of these factors will lead to a difference in the adsorption of C=O groups of methyl laurate and intermediate oxygenates (such as lauric acid and lauraldehyde) on Ni-Zn alloys and IMCs from that on metallic Ni.

It has been proposed that when ester, acid and aldehyde are adsorbed on the metal surface, there are three configurations, i.e.,  $\eta^1(\text{C})$ -acyl,  $\eta^2(\text{C},\text{O})$ -aldehyde and carboxylate (Scheme 2) [60]. The  $\eta^1(\text{C})$ -acyl group preferentially forms on the metal surface [60–62], and it either directly decarbonylates/decarboxylates to produce CO/ $\text{CO}_2$  and hydrocarbon or is hydrogenated to yield alcohol. Actually, decarbonylation/decarboxylation have been found to prevail on noble metals and Ni [3,10,18,20]. Here, we suggest that on the surface of Ni-Zn alloy and IMCs, the presence of Zn favors the adsorption of  $\eta^2(\text{C},\text{O})$ -aldehyde rather than  $\eta^1(\text{C})$ -acyl, where C and O atoms preferentially adsorb on Ni and Zn atoms, respectively. This finding is reasonable because Zn is more oxophilic, while Ni has a high affinity to carbon [21,63]. With decreasing Ni/Zn ratios, the  $\eta^2(\text{C},\text{O})$ -aldehyde configuration would be more and more favored due to the increased amount of surface Zn atoms. At Ni/Zn ratios  $\leq 2$ , t-NiZn and c-NiZn IMCs are expected to be the most appropriate situation for the  $\eta^2(\text{C},\text{O})$ -aldehyde configuration. Compared to  $\eta^1(\text{C})$ -acyl,  $\eta^2(\text{C},\text{O})$ -aldehyde is more easily attacked by H species to produce alcohol, followed by dehydration/hydrogenation and/or C–O bond hydrogenolysis to yield hydrocarbon. Accordingly, a synergetic effect occurred between the surface Ni and Zn atoms for the activation of the C=O group. This finding can also account for higher TOF of methyl laurate on the  $\text{Ni}_x\text{Zn}_y\text{Al}$  catalysts with Ni/Zn ratios  $\leq 2/1$  compared to that on  $\text{Ni}_3\text{Zn}_0\text{Al}$ . Similarly, the addition of more oxophilic metals like Zn to Pt [22,23], Fe to Pt [64] and Fe to Ni [65] have been found to facilitate the  $\eta^2(\text{C},\text{O})$  configuration. Compared to the Pt(111) surface where aldehydes adsorb in the  $\eta^1(\text{C})$ -acyl configuration, the bimetallic Zn/Pt(111) surface favors the adsorption of aldehydes in the  $\eta^2(\text{C},\text{O})$  configuration, followed by selective C–O bond cleavage to produce hydrocarbon [22,23]. Li et al. [21] reported that the formation

Scheme 2. Important oxygenate intermediates on transition metal surfaces [60].



of Ni–Zn alloy facilitates C–O bond cleavage in the hydrogenolysis of glycerol, which is attributed to the adsorption of hydroxyl groups on the oxophilic Zn sites activating the C–O bond. Because of the higher affinity of Fe to oxygen [66], the Ni–Fe bimetallic catalysts have been found to favor the HDO pathway in the deoxygenation of fatty acid esters [15,16]. Based on density functional theory (DFT) calculations for aldehyde adsorption on Ni–Fe/SiO<sub>2</sub>, Sitthisa et al. [65] proposed that the Fe atoms preferentially bond the oxygen in carbonyl to form the  $\eta^2(\text{C},\text{O})$  configuration, leading to a weakening of the C–O bond and facilitating its dissociation to produce 2-methylfuran. This finding is very different from the performance of the Ni/SiO<sub>2</sub> catalyst that was highly selective for decarbonylation of furfural to produce furan (C<sub>4</sub>H<sub>4</sub>O) and CO. Based on its oxophilicity, Fe has also been used for promoting the selective cleavage of the C–O bond in phenolic compounds by forming bimetallic NiFe and PdFe alloys [15,67,68]. In short, introducing the less reactive and more oxophilic Zn into a metallic Ni-forming alloys and IMCs favors the adsorption of methyl laurate and its oxygenated intermediates in the  $\eta^2(\text{C},\text{O})$  configuration, and subsequently promotes the HDO pathway.

Additionally, the electron density of the Ni atom also affects decarbonylation/decarboxylation. It is well accepted that the cleavage of the  $\beta$  C–H bond is the rate-determining step in the decarbonylation of  $\eta^1(\text{C})$ -acyl or the decarboxylation of carboxylate [62,65,69], and it is facilitated by increasing the electron density of the metal site [69,70]. Our previous work [10] indicates that in metallic Ni and Ni phosphides, the higher the electron density of the Ni site, the more dominating the decarbonylation/decarboxylation pathway. In the present work, a small charge transfer from Ni to Zn was found in the Ni–Zn alloys and IMCs, i.e., the electron density of the Ni site was reduced. From the CO-TPD results (Fig. 7), the electron density of the Ni atom tended to decrease with decreasing Ni/Zn ratios. Consequently, decarbonylation/decarboxylation was greatly suppressed with decreasing Ni/Zn ratios. Similarly, the bimetallic Zn/Pt(111) surface had a higher barrier for C–H bond cleavage than Pt(111), which is ascribed to a charge transfer from Pt to Zn [22,26].

In summary, both the high oxophilicity of Zn atoms and the decrease in the electron density of Ni atoms contributed to promoting the HDO pathway and suppressing the decarbonylation/decarboxylation pathway. This finding is more obvious when Ni–Zn IMCs formed in Ni<sub>x</sub>Zn<sub>y</sub>Al with Ni/Zn ratios  $\leq 2/1$ .

#### 4.3. C–C bond hydrogenolysis and methanation

As introduced in Section 3.2, the formation of Ni–Zn alloys and IMCs suppressed C–C bond hydrogenolysis, especially the formation of IMCs. This finding is more obviously reflected by the performance of Ni<sub>x</sub>Zn<sub>y</sub>Al with Ni/Zn ratios  $\leq 2/1$  at 400 °C, where  $S_{\text{C}_{11}+\text{C}_{12}}$  was above 90%. However,  $S_{\text{C}_{11}+\text{C}_{12}}$  was close to zero on Ni<sub>x</sub>Zn<sub>y</sub>Al, with Ni/Zn ratios  $\geq 3/1$  at 400 °C. It has been widely accepted that the large ensembles of Ni sites are favorable for C–C bond hydrogenolysis [71], and the co-adsorption of two adjacent atoms is required to facilitate C–C bond cleavage [71]. Because the Zn atom possesses a reduced ability for adsorbing the hydrocarbons compared to nickel, the reduced ensemble of Ni atoms on Ni–Zn alloys and IMCs could be unfavorable for the adsorption of hydrocarbon and thus C–C bond cleavage. A similar case was also found with Ni–Cu and Ni–Fe bimetallic catalysts [16,19]. Apart from geometric factors, the decrease in the electron density of Ni atoms was also negative for C–C bond hydrogenolysis. Referring to the hydrogenolysis mechanism of ethane [71], the first step is the C–H bond cleavage yielding a hydrogen-deficient dicarbon species, while the low electron density is not beneficial to the activation of the C–H bond [69,70].

As shown in Fig. 11, the  $(\text{CO} + \text{CO}_2)/\text{C}_{11}$  ratio was zero or close to zero even at 330 °C on Ni<sub>3</sub>Zn<sub>0</sub>Al, Ni<sub>50</sub>Zn<sub>1</sub>Al and Ni<sub>8</sub>Zn<sub>1</sub>Al, which is indicative of the complete methanation of CO/CO<sub>2</sub>. In comparison, when the Ni/Zn atomic ratio was  $\leq 4/1$ , the  $(\text{CO} + \text{CO}_2)/\text{C}_{11}$  ratio

increased. Particularly, for the catalysts with Ni/Zn ratios  $\leq 2/1$ , the  $(\text{CO} + \text{CO}_2)/\text{C}_{11}$  ratio was larger than 1.0 even at 400 °C. Table 2 shows that Ni<sub>1</sub>Zn<sub>1</sub>Al showed very low methanation reactivity even at 400 °C. The formation of IMCs (i.e., c-NiZn and t-NiZn) is essential for remarkably suppressing methanation. This finding should be attributed to the geometric and electronic effects of Zn in IMCs. On one hand, the ensemble of Ni sites on IMCs is expected to be smaller than that on metallic Ni or Ni-rich alloys. This finding is unfavorable for the activation of CO/CO<sub>2</sub>. On the basis of DFT calculations, Ni monomers on Cu (111) have been found to have higher energy barriers than Ni dimers and trimers for the dissociation of the C–O bond of CO [72]. On the other hand, the decreased electron density of the Ni sites could weaken  $\pi$  back-donation from the occupied bands of Ni into the  $\text{CO}(2\pi^*)$  orbitals [26]. Consequently, the dissociation of the C–O bond is suppressed. Similarly, different from the metallic Ni that favored methanation, the NiZn IMC mainly facilitated the decomposition of methanol to CO and H<sub>2</sub> in the steam reforming of methanol [25]. The suppression of the electron-deficient Ni on methanation was also found for NiCe<sub>1-x</sub>Ni<sub>x</sub>O<sub>2-y</sub> in ethanol steam reforming [73]. In contrast, the introduction of boron into metallic Ni promoted methanation due to a charge transfer from boron to Ni [74].

In conclusion, the geometric and electronic effects of Zn in the Ni–Zn alloys and IMCs can account for the suppression of C–C bond hydrogenolysis and methanation on Ni<sub>x</sub>Zn<sub>y</sub>Al catalysts. Particularly, the formation of IMCs is more vital.

## 5. Conclusion

The structure of Ni<sub>x</sub>Zn<sub>y</sub>Al bimetallic catalysts prepared from layered double hydroxides was dependent on the Ni/Zn atomic ratios. After layered double hydroxides were calcined at 500 °C in air and reduced with H<sub>2</sub> at 650 °C, Ni-rich alloy and Ni–Zn IMC were synthesized at an Ni/Zn atomic ratio larger and less than 2. With decreasing Ni/Zn ratios, the Ni-rich alloy and Ni–Zn IMC crystallite sizes slightly increased, while H<sub>2</sub> uptakes remarkably decreased. HAADF-STEM, H<sub>2</sub> chemisorption and magnetic measurement results show that the Ni and Zn atoms were homogeneously distributed in the catalyst, while XPS and CO-TPD characterizations revealed a charge transfer from Ni to Zn. Zn geometrically and electronically modified Ni, which became greater with decreasing Ni/Zn ratios.

In the deoxygenation of methyl laurate as a model compound to diesel-like hydrocarbons, the Ni–Zn bimetallic catalysts showed lower conversion than the metallic Ni due to the decrease in the surface Ni site density, while the synergetic effect between Ni and Zn led to higher TOF. Different from metallic Ni, due to the higher oxophilicity of Zn, Ni-rich alloys and Ni–Zn IMCs favor the HDO pathway more, which is more remarkable with decreasing Ni/Zn atomic ratios. Meaningfully, C–C bond hydrogenolysis and methanation were suppressed due to the formation of Ni-rich alloys and Ni–Zn IMCs, especially that of Ni–Zn IMC. These results are ascribed to the geometric and electronic effects of Zn on Ni. Given the low reactivity for C–C bond hydrogenolysis and methanation, we propose that the Ni–Zn IMC is very promising for the deoxygenation of fatty acid esters to diesel-like hydrocarbons with high carbon yield and low H<sub>2</sub> consumption.

## Acknowledgement

The authors gratefully acknowledge support from the National Natural Science Foundation of China (No. 21576193 and 21176177).

## Appendix A. Supplementary data

Supplementary data associated with this article can be found, in the online version, at <http://dx.doi.org/10.1016/j.apcatb.2017.10.040>.



## References

- [1] D. Kubička, L. Kaluža, Deoxygenation of vegetable oils over sulfided Ni, Mo and NiMo catalysts, *Appl. Catal. A-Gen.* 372 (2010) 199–208.
- [2] S. Lestari, P. Mäki-Arvela, J. Beltramini, G.Q.M. Lu, D.Y. Murzin, Transforming triglycerides and fatty acids into biofuels, *ChemSusChem* 2 (2009) 1109–1119.
- [3] M. Šnāre, I. Kubičková, P. Maľki-Arvela, K. Eränen, D.Y. Murzin, Heterogeneous catalytic deoxygenation of stearic acid for production of biodiesel, *Ind. Eng. Chem. Res.* 45 (2006) 5708–5715.
- [4] C. Kordulis, K. Bourikas, M. Gousi, E. Kordouli, A. Lycourghiotis, Development of nickel based catalysts for the transformation of natural triglycerides and related compounds into green diesel: a critical review, *Appl. Catal. B-Environ.* 181 (2016) 156–196.
- [5] L. Di, S. Yao, S. Song, G. Wu, W. Dai, N. Guan, L. Li, Robust ruthenium catalysts for the selective conversion of stearic acid to diesel-range alkanes, *Appl. Catal. B-Environ.* 201 (2017) 137–149.
- [6] A.E. Coumans, E.J.M. Hensen, A model compound (methyl oleate oleic acid, triolein) study of triglycerides hydrodeoxygenation over alumina-supported NiMo sulfide, *Appl. Catal. B-Environ.* 201 (2017) 290–301.
- [7] C. Dupont, R. Lemeur, A. Daudin, P. Raybaud, Hydrodeoxygenation pathways catalyzed by MoS<sub>2</sub> and NiMoS active phases: a DFT study, *J. Catal.* 279 (2011) 276–286.
- [8] E. L. Kordouli, C. Sygellou, K. Kordulis, A. Bourikas, A. Lycourghiotis, Probing the synergistic ratio of the NiMo/γ-Al<sub>2</sub>O<sub>3</sub> reduced catalysts for the transformation of natural triglycerides into green diesel, *Appl. Catal. B-Environ.* 209 (2017) 12–22.
- [9] T. Morgan, E. Santillan-Jimenez, A.E. Harman-Ware, Y. Ji, D. Grubb, M. Crocker, Catalytic deoxygenation of triglycerides to hydrocarbons over supported nickel catalysts, *Chem. Eng. J.* 181–190 (2012) 346–355.
- [10] J. Chen, H. Shi, L. Li, K. Li, Deoxygenation of methyl laurate as a model compound to hydrocarbons on transition metal phosphide catalysts, *Appl. Catal. B-Environ.* 144 (2014) 870–884.
- [11] Z. Pan, R. Wang, M. Li, Y. Chu, J. Chen, Deoxygenation of methyl laurate to hydrocarbons on silica-supported Ni-Mo phosphides: effect of calcination temperatures of precursor, *J. Energ. Chem.* 24 (2015) 77–86.
- [12] V. Ponec, Alloy catalysts: the concepts, *Appl. Catal. A-Gen.* 222 (2001) 31–45.
- [13] B. Coq, F. Figueras, Structure–activity relationships in catalysis by metals: some aspects of particle size, bimetallic and supports effects, *Coord. Chem. Rev.* 178–180 (1998) 1753–1783.
- [14] M. Armbrüster, R. Schlögl, Y. Grin, Intermetallic compounds in heterogeneous catalysis—a quickly developing field, *Sci. Technol. Adv. Mater.* 15 (2014) 034803.
- [15] S. Leng, X. Wang, X. He, L. Liu, Y. Liu, X. Zhong, G. Zhuang, J. Wang, NiFe/γ-Al<sub>2</sub>O<sub>3</sub>: A universal catalyst for the hydrodeoxygenation of bio-oil and its model compounds, *Catal. Commun.* 41 (2013) 34–37.
- [16] X. Yu, J. Chen, T. Ren, Promotional effect of Fe on performance of Ni/SiO<sub>2</sub> for deoxygenation of methyl laurate as a model compound to hydrocarbons, *RSC Adv.* 4 (2014) 46427–46436.
- [17] A.L. Kustov, A.M. Frey, T. Larsen, J.K. Nørskov, C.H. Christensen, CO methanation over supported bimetallic Ni-Fe catalysts: from computational studies towards catalyst optimization, *Appl. Catal. A-Gen.* 320 (2007) 98–104.
- [18] R. Loe, E. Santillan-Jimenez, T. Morgan, L. Sewell, Y. Ji, S. Jones, M.A. Isaacs, A.F. Lee, M. Crocker, Effect of Cu and Sn promotion on the catalytic deoxygenation of model and algal lipids to fuel-like hydrocarbons over supported Ni catalysts, *Appl. Catal. B-Environ.* 191 (2016) 147–156.
- [19] V.A. Yakovlev, S.A. Khromova, O.V. Sherstnyuk, V.O. Dundich, D.Y. Ermakov, V.M. Novopashina, M.Y. Lebedev, O. Bulavchenko, V.N. Parmon, Development of new catalytic systems for upgraded bio-fuels production from bio-crude-oil and biodiesel, *Catal. Today* 144 (2009) 362–366.
- [20] R.G. Kukulshkin, O.A. Bulavchenko, V.V. Kaichev, V.A. Yakovlev, Influence of Mo on catalytic activity of Ni-based catalysts in hydrodeoxygenation of esters, *Appl. Catal. B-Environ.* 163 (2015) 531–538.
- [21] X. Li, C. Zhang, H. Cheng, L. He, W. Lin, Y. Yu, F. Zhao, Effect of Zn doping on the hydrogenolysis of glycerol over ZnNiAl Catalyst, *J. Mol. Catal. A-Chem.* 395 (2014) 1–6.
- [22] J.R. McManus, E. Martono, J.M. Vohs, Selective deoxygenation of aldehydes: the reaction of acetaldehyde and glycolaldehyde on Zn/Pt(111) bimetallic surfaces, *ACS Catal.* 3 (2013) 1739–1750.
- [23] D. Shi, J.M. Vohs, Deoxygenation of biomass-derived oxygenates: reaction of furfural on Zn-modified Pt(111), *ACS Catal.* 5 (2015) 2177–2183.
- [24] L. Yang, Z. Jiang, G. Fan, F. Li, The promotional effect of ZnO addition to supported Ni nanocatalysts from layered double hydroxide precursors on selective hydrogenation of citral, *Catal. Sci. Technol.* 4 (2014) 1123–1131.
- [25] S. Kameoka, T. Kimura, A.P. Tsai, A novel process for preparation of unsupported mesoporous intermetallic NiZn and PdZn catalysts, *Catal. Lett.* 131 (2009) 219–224.
- [26] J.A. Rodriguez, M. Kuhn, Interaction of zinc with transition-metal surfaces: electronic and chemical perturbations induced by bimetallic bonding, *J. Phys. Chem.* 100 (1996) 381–389.
- [27] G. Fan, F. Li, D.G. Evans, X. Duan, Catalytic applications of layered double hydroxides: recent advances and perspectives, *Chem. Soc. Rev.* 43 (2014) 7040–7066.
- [28] C. Li, M. Wei, D.G. Evans, X. Duan, Layered double hydroxide-based nanomaterials as highly efficient catalysts and adsorbents, *Small* 10 (2014) 4469–4486.
- [29] S. He, Z. An, M. Wei, D.G. Evans, X. Duan, Layered double hydroxide-based catalysts: nanostructure design and catalytic performance, *Chem. Commun.* 49 (2013) 5912–5920.
- [30] Z. Pan, R. Wang, Z. Nie, J. Chen, Effect of a second metal (Co, Fe Mo and W) on performance of Ni<sub>2</sub>P/SiO<sub>2</sub> for hydrodeoxygenation of methyl laurate, *J. Energy Chem.* 25 (2016) 418–426.
- [31] J.A. Cecilia, A. Infantes-Molina, E. Rodríguez-Castellón, A. Jiménez-López, S.T. Oyama, Oxygen-removal of dibenzofuran as a model compound in biomass derived bio-oil on nickel phosphide catalysts: role of phosphorus, *Appl. Catal. B-Environ.* 136–137 (2013) 140–149.
- [32] M.N. Barroso, M.F. Gomez, L.A. Arrúa, M.C. Abello, Hydrogen production by ethanol reforming over NiZnAl catalysts, *Appl. Catal. A-Gen.* 304 (2006) 116–123.
- [33] K.M. Lee, W.Y. Lee, Partial oxidation of methane to syngas over calcined Ni–Mg/Al layered double hydroxides, *Catal. Lett.* 83 (2002) 65–70.
- [34] A. Zhao, W. Ying, H. Zhang, H. Ma, D. Fang, Ni–Al<sub>2</sub>O<sub>3</sub> catalysts prepared by solution combustion method for syngas methanation, *Catal. Commun.* 17 (2012) 34–38.
- [35] J. Van De Loosdrecht, A.M. Van Der Kraan, A.J. van Dillen, J.W. Geus, Metal-support interaction: titania-supported and silica-supported nickel catalysts, *J. Catal.* 170 (1997) 217–226.
- [36] Z. Boukha, C. Jiménez-González, B.D. Rivas, J.R. González-Velasco, J.I. Gutiérrez-Ortiz, R. López-Fonseca, Synthesis characterisation and performance evaluation of spinel-derived Ni/Al<sub>2</sub>O<sub>3</sub> catalysts for various methane reforming reactions, *Appl. Catal. B-Environ.* 158–159 (2014) 190–201.
- [37] C.S. Spanjers, J.T. Held, M.J. Jones, D.D. Stanley, R.S. Sim, M.J. Janik, R.M. Rioux, Zinc inclusion to heterogeneous nickel catalysts reduces oligomerization during the semi-hydrogenation of acetylene, *J. Catal.* 316 (2014) 164–173.
- [38] S. Jana, J.W. Chang, R.M. Rioux, Synthesis and modeling of hollow intermetallic Ni–Zn nanoparticles formed by the Kirkendall effect, *Nano. Lett.* 13 (2013) 3618–3625.
- [39] T. Sakamoto, D. Matsumura, K. Asazawa, U. Martinez, A. Serov, K. Artyushkova, P. Atanassov, K. Tamura, Y. Nishihata, H. Tanaka, Operando XAFS study of carbon supported Ni, NiZn and Co catalysts for hydrazine electrooxidation for use in anion exchange membrane fuel cells, *Electrochim. Acta* 163 (2015) 116–122.
- [40] M. Friedrich, D. Teschner, A. Knop-Gericke, M. Armbrüster, Surface and subsurface dynamics of the Intermetallic compound ZnNi in methanol steam reforming, *J. Phys. Chem. C* 116 (2012) 14930–14935.
- [41] J.H. Hwang, V.P. Dravid, M.H. Teng, J.J. Host, B.R. Elliott, D.L. Johnson, T.O. Mason, Magnetic properties of graphically encapsulated nickel nanocrystals, *J. Mater. Res.* 12 (1997) 1076–1082.
- [42] J.L. Carter, J.H. Sinfelt, Catalysis over supported metals. VI. The application of magnetic studies in the interpretation of the catalytic properties of nickel, *J. Phys. Chem.* 70 (1966) 3003–3006.
- [43] J.L. Carter, J.A. Cusumano, J.H. Sinfelt, Catalysis over supported metals. V. The effect of crystallite size on the catalytic activity of nickel, *J. Phys. Chem.* 70 (1966) 2257–2263.
- [44] A.C. Hegde, K. Venkatakrishna, N. Eliaz, Electrodeposition of zn-Ni, zn-Fe and Zn-Ni-Fe alloys, *Surf. Coat. Tech.* 205 (2010) 2031–2041.
- [45] S.W. Gaarenstroom, N. Winograd, Initial and final state effects in the ESCA spectra of cadmium and silver oxides, *J. Chem. Phys.* 67 (1977) 3500–3506.
- [46] S.P. Kowalczyk, L. Ley, F.R. McFeely, R.A. Pollak, D.A. Shirley, Relative effect of extra-atomic relaxation on Auger and binding-energy shifts in transition metals and salts, *Phys. Rev. B* 9 (1974) 381–391.
- [47] J.A. Rodriguez, Physical and chemical properties of bimetallic surfaces, *Surf. Sci. Rep.* 24 (1996) 223–287.
- [48] G. Blyholder, Molecular orbital view of chemisorbed carbon monoxide, *J. Phys. Chem.* 68 (1964) 2772–2777.
- [49] K. Hermann, P.S. Bagus, C.J. Nelin, Size dependence of surface cluster models: CO adsorbed on Cu(100), *Phys. Rev. B* 35 (1987) 9467–9473.
- [50] E.R. Davidson, K.L. Kunze, F.B.C. Machado, S.J. Chakravorty, The transition metal-carbonyl bond, *Accounts Chem. Res.* 26 (1993) 628–635.
- [51] B. Hammer, Y. Morikawa, J.K. Nørskov, CO chemisorption at metal surfaces and overlayers, *Phys. Rev. Lett.* 76 (1996) 2141–2144.
- [52] J.A. Rodriguez, D.W. Goodman, The nature of the metal–metal bond in bimetallic surfaces, *Science* 257 (1992) 897–903.
- [53] J.A. Rodriguez, Interactions in bimetallic bonding: electronic and chemical properties of PdZn surfaces, *J. Phys. Chem.* 98 (1994) 5758–5764.
- [54] O.I. Senol, T.R. Viljava, A.O.I. Krause, Hydrodeoxygenation of methyl esters on sulphided NiMo/γ-Al<sub>2</sub>O<sub>3</sub> and CoMo/γ-Al<sub>2</sub>O<sub>3</sub> catalysts, *Catal. Today* 100 (2005) 331–335.
- [55] B. Donnis, R.G. Egeberg, P. Blom, K.G. Knudsen, Hydroprocessing of bio-oils and oxygenates to hydrocarbons. Understanding the reaction routes, *Top. Catal.* 52 (2009) 229–240.
- [56] B. Hovecar, M. Grilc, M. Hus, B. Likozar, Mechanism, ab initio calculations and microkinetics of hydrogenation, hydrodeoxygenation, double bond migration and cis-trans isomerisation during hydrotreatment of C<sub>6</sub> secondary alcohol species and ketones, *Appl. Catal. B-Environ.* 218 (2017) 147–162.
- [57] K. Kovnir, M. Armbrüster, D. Teschner, T.V. Venkov, F.C. Jentoft, A. Knop-Gericke, Y. Grin, R. Schlögl, A new approach to well-defined, stable and site-isolated catalysts, *Sci. Technol. Adv. Mat.* 8 (2007) 420–427.
- [58] K. Thirunavukkarasu, T.M. Sankaranarayanan, A. Pandurangan, R.V. Shanthi, S. Sivasanker, The role of surface Zn<sup>2+</sup> ions in the transesterification of vegetable oils over ZnO supported on Al<sub>2</sub>O<sub>3</sub> and Fe<sub>2</sub>O<sub>3</sub>, *Catal. Sci. Technol.* 4 (2014) 851–860.
- [59] Q. Liu, L. Wang, C. Wang, W. Qu, Z. Tian, H. Ma, D. Wang, B. Wang, Z. Xu, The effect of lanthanum doping on activity of Zn-Al spinel for transesterification, *Appl. Catal. B-Environ.* 136–137 (2013) 210–217.
- [60] M. Mavrikakis, M.A. Barteau, Oxygenate reaction pathways on transition metal surfaces, *J. Mol. Catal. A-Chem.* 131 (1998) 135–147.
- [61] E. Zahidi, M. Castonguay, P. McBreen, RAIRS and TPD study of methyl formate ethyl formate, and methyl acetate on Ni (111), *J. Am. Chem. Soc.* 116 (1994) 5847–5856.

- [62] J.L. Davis, M.A. Barteau, Polymerization and decarbonylation reactions of aldehydes on the Pd (111) surface, *J. Am. Chem. Soc.* 111 (1989) 1782–1792.
- [63] C.H. Bartholomew, Carbon deposition in steam reforming and methanation, *Catal. Rev.* 24 (1982) 67–112.
- [64] F. Hirschl, P. Delbecq, J. Sautet, Adsorption of unsaturated aldehydes on the (111) surface of a Pt–Fe alloy catalyst from first principles, *J. Catal.* 217 (2003) 354–366.
- [65] S. Sitthitha, W. An, D.E. Resasco, Selective conversion of furfural to methylfuran over silica-supported Ni–Fe bimetallic catalysts, *J. Catal.* 284 (2011) 90–101.
- [66] R. Pestman, R.M. Koster, J.A.Z. Pieterse, V. Ponc, Reactions of carboxylic acids on oxides: 1. Selective hydrogenation of acetic acid to acetaldehyde, *J. Catal.* 168 (1997) 255–264.
- [67] J. Sun, A.M. Karim, H. Zhang, L. Kovarik, X.S. Li, A.J. Hensley, J.S. McEwen, Y. Wang, Carbon-supported bimetallic Pd–Fe catalysts for vapor-phase hydrodeoxygenation of guaiacol, *J. Catal.* 306 (2013) 47–57.
- [68] L. Nie, P.M. de Souza, W. Noronha, T. An, D.E. Resasco, Selective conversion of m-cresol to toluene over bimetallic Ni–Fe catalysts, *J. Mol. Catal. A-Chem.* 388–389 (2014) 47–55.
- [69] V. Pallassana, M. Neurock, Reaction paths in the hydrogenolysis of acetic acid to ethanol over Pd (111) Re (0001), and PdRe alloys, *J. Catal.* 209 (2002) 289–305.
- [70] V. Pallassana, M. Neurock, Electronic factors governing ethylene hydrogenation and dehydrogenation activity of pseudomorphic Pd ML/Re (0001), Pd ML/Ru (0001) Pd (111), and Pd ML/Au (111) surfaces, *J. Catal.* 191 (2000) 301–317.
- [71] J.H. Sinfelt, Catalysis by alloys and bimetallic clusters, *Accounts Chem. Res.* 10 (1977) 15–20.
- [72] L.Y. Gan, R.Y. Tian, X.B. Yang, H.D. Lu, Y.J. Zhao, Catalytic reactivity of CuNi alloys toward H<sub>2</sub>O and CO dissociation for an efficient water-gas shift: a DFT study, *J. Phys. Chem. C* 116 (2012) 745–752.
- [73] L. Zhou, S. Barrio, J. Senanayake, A. Evans, M. Kubacka, J.C. Hanson, A. Martínez-Arias, M. Fernández-García, J.A. Rodríguez, High activity of Ce<sub>1-x</sub>Ni<sub>x</sub>O<sub>2-y</sub> for H<sub>2</sub> production through ethanol steam reforming: tuning catalytic performance through metal–oxide interactions, *Angew. Chem. Int. Ed.* 49 (2010) 9680–9684.
- [74] Y. Okamoto, E. Matsunaga, T. Imanaka, S. Teranishi, Surface state and catalytic activity and selectivity of nickel catalysts in hydrogenation reactions: V. Electronic effects on methanation of CO and CO<sub>2</sub>, *J. Catal.* 74 (1982) 183–187.